

International Space Station Leak Localization Using Attitude Disturbance Estimation

Jong-Woo Kim, John L. Crassidis
Department of Mechanical and Aerospace Engineering
University at Buffalo, The State University of New York
Amherst, NY 14260-4400
716-645-2593 ext. 2246
jk45@eng.buffalo.edu, johnc@eng.buffalo.edu

Srinivas R. Vadali
Department of Aerospace Engineering
Texas A&M University
College Station, TX 77843-3141
979-845-6051
svadali@aero.tamu.edu

Adam L. Dershowitz
United Space Alliance
NASA Johnson Space Center, Code DF64
Houston, TX 77058
281-483-5410
adam.dershowitz1@jsc.nasa.gov

Abstract—In this paper we present a new method to localize air leaks on the International Space Station based on the spacecraft attitude and rate behavior produced by a mass expulsion force of the leaking air. Thrust arising from the leak generates a disturbance torque, which is estimated using a real-time filter with a dynamical model (including external disturbances such as aerodynamic drag and gravity-gradient). The leak location can be found by estimating the moment arm of the estimated disturbance torque, assuming that leak is caused by only one hole. Knowledge of the leak thrust magnitude and its resulting disturbance torque are needed to estimate the moment arm. The leak thrust direction is assumed to be perpendicular to the structure surface and its magnitude is determined using a Kalman filter with a nozzle dynamics model. There may be multiple leak locations for a given response, but the actual geometric structure of the space station eliminates many of the possible solutions. Numerical results show that the leak localization method is very efficient when used with the conventional sequential hatch closure or airflow induction sensor system.

TABLE OF CONTENTS

1	INTRODUCTION
2	PRELIMINARIES
3	ESTIMATION OF VENT THRUST MAGNITUDE
4	UNSCENTED FILTER

5	PARAMETER ESTIMATION
6	LEAK LOCALIZATION
7	NUMERICAL SIMULATION
8	EXPERIMENTAL VALIDATION
9	CONCLUSIONS
10	ACKNOWLEDGEMENTS

1. INTRODUCTION

The International Space Station (ISS) is orbiting in a 51.6° inclination near-circular Low-Earth-Orbit (LEO) with an altitude between 370 and 460 km, and is expected to have a minimum operational lifetime of 15 years. Because of the large structure, long lifetime and orbit characteristics [1], the ISS may be subject to impacts of hyper velocity particles such as micro-meteorites and space debris that can severely damage the station. This damage may threaten the safety of the crew if the pressurized wall of a module is perforated, which may result in significant air loss. Collisions with other objects are another possible cause of a leak, as occurred in the Russian Space Station Mir in 1997. To protect the ISS from the impact damages, various debris shields have been designed. Heavy shields are placed in the forward facing area which is likely to be hit frequently, and fewer shields are used in the nadir-facing and aft area [2].

Perforations in a pressurized module will result in a rapid temperature and pressure decrease. Therefore fast determination of the extent and location of the leak is needed to maintain the operational status in order to provide safety for

the crew. The first indication of a leak in the ISS is the depressurization of a module. The leak size can be calculated by measuring the internal pressure and its depressurization rate. Based on the extent of leak it is possible to calculate the “reserve time” left until a crew evacuation is required. Depending on the reserve time operational decisions must be made, including: 1) whether or not to perform a leak isolation to patch the leak, or 2) evacuate the ISS. Leak localization should be performed first to find the leaking module. Then the exact location within the leaking module for repair purposes can be determined.

Conventional methods to locate air leaks on the ISS include the sequential module leak isolation process for the US segment (prior to assembly stage 10A) and the airflow induction sensor system for the Russian segment. The sequential module leak isolation process involves having the crew close hatches sequentially while monitoring the pressure difference across each hatch. A drawback of this process is very small pressure differences can keep a closed hatch from being open again, which significantly reduces the reserve time and can pose an immediate risk to the crew. Thus, safety dictates that the hatches be closed in an order that will never trap a crew member away from the escape vehicle. This may significantly inhibit the leak isolation process if the leaking module is not located within the first few hatch closures.

The airflow induction sensor system employs hot-wire anemometers situated in hatchways to measure the air flow direction and its rate. The hot-wire anemometer operates by air passing across a wire with a current running through it to maintain a constant temperature in the wire. These devices are installed at all hatchways of the Russian segments. However, the airflow induction sensor system designed for the ISS has several limitations for the following reasons. The sensors are not mounted at all hatchways of the US segment (only at Node-2 and Node-3 of the US segment). Therefore the sequential module isolation process is still needed to determine which module leaks in the US segments. Since the sensors are very sensitive to the air circulation inside, the venting system and the movement of the crew must be stopped for several minutes, which may waste time in an emergency situation. Because these sensors are situated in hatchways, the location of the leak within the suspected leaking module cannot be found for repair purposes without using other inspection processes (this is also true for the sequential isolation process). Therefore a more efficient localization system is needed to locate the leaks.

The new method presented in this paper uses the attitude response of the ISS caused by the leak reaction force of the air flowing through a perforated hole. The vent thrust can yield a strong reaction torque depending on the size and location of the leak. A leak hole on the surface of a pressurized module can be modeled as a short nozzle with the leaking air as the propellant. We assume that the line of action of the vent thrust is perpendicular to the cross section

area of the leak hole. This assumption is reasonable due to the relatively thin skin of each module. Based on the nozzle dynamics, an extended Kalman filter (EKF) algorithm is used to estimate the vent thrust magnitude with the internal pressure measurements. The venting torque is estimated by the Unscented Filter (UF) developed by Julier and Uhlman [3]. Since the external attitude-dependent disturbance torque (gravity-gradient and aerodynamic torque) are functions of the attitude of the spacecraft, a new attitude filtering approach called the Unscented Quaternion Estimator (USQUE) developed by Crassidis and Markley [4] is employed. The advantages of the UF are: 1) it captures the posterior mean and covariance of a random variable accurately to the second-order Taylor series expansion for any nonlinearity by choosing a minimal set of sample points and propagating them through the original nonlinear system, 2) it is derivative-free, i.e. no Jacobian and Hessian calculations need to be evaluated for the computation which enable the UF to be applied to any complex dynamical system and to non-differentiable functions [5]. The vent torque, which is not explicitly modeled in the attitude dynamics, shows up as a residual disturbance torque when the spacecraft angular rate measurement undergoes a filtering process. In the disturbance torque estimation algorithm, the filter state vector is augmented to include the unknown parameters as additional states, resulting in a total of six states, where three states are for the angular rate or angular momentum of the spacecraft and the remaining three states are for the 3-axis components of the disturbance torque. But problems arise when the unmodeled dynamics (besides the vent torque) dominate the residual torque.

Among the external disturbances, the gravity-gradient torque can be treated as a well-known quantity if the inertia of the spacecraft is well known, whereas the aerodynamic torque has large uncertainties in its parameters. Also, problems may arise in the accuracy of the vent torque estimates when significant inertia modeling errors of the spacecraft are present. Therefore parameter estimation methods should be employed to estimate these uncertainties when we know that there is not a venting leak acting on the spacecraft. A real-time parameter estimation algorithm to estimate the inertia and the aerodynamic torque is developed in this paper by employing the UF approach. But the parameter estimation performance depends heavily on the observability of the parameters of interest. Therefore some simple observability tests are done to measure the relative observability of the unknown parameters. It is shown that the complete inertia parameters are unobservable when the space station attitude is in its torque equilibrium attitude (TEA), which is the nominal ISS operational attitude. But the inertia observability can be strengthened with the presence of attitude maneuvers. Problems in estimating uncertain inertia and external disturbance torque for the ISS are investigated in several papers such as Refs. [6] and [7]. In Ref. [8], small sinusoidal probing signals are used to enhance the observability of the inertia by causing attitude motion about the TEA. Also in Ref. [7], the estimation algorithm to determine the mass and aerodynamic torque proper-

ties of the ISS in Low-Earth Orbit (LEO) based on the least-square method has been derived with the use of an indirect adaptive control algorithm to enhance the observability of the unknown parameters. This method uses a smoothing method to estimate the unmeasured angular acceleration.

The possible locations of the air leak are then calculated using the estimated vent torque, vent thrust magnitude, and the actual geometric structure of the pressurized segments. For simplicity, the disturbance torque caused by the pressure of the impingement of the leaking air plume on nearby surfaces is neglected. Also, we assume that the leak is caused by a single leak hole. There may be single or multiple leak locations that produce the same attitude response. To reduce the number of possible solutions, conventional methods are combined with the new leak localization method. This approach reduces the number of possible solutions, so that fewer hatch closures are required to uniquely determine the leak location. Advantages of the attitude response method include:

1. No other devices are needed besides pressure gauges to measure the air pressure, and spacecraft attitude and rate sensors.
2. Relatively fast leak localization can be achieved compared to the conventional leak localization method proposed for the ISS.
3. The new method not only determines the possible leaking modules but also determines the possible locations of the leak hole within those modules. This may be critical to allow for repairs rather than sealing off a module or performing a station evacuation.

The remainder of paper is organized as follows. First, a summary of the attitude kinematics and dynamics for the ISS is given. Next, using the isentropic nozzle theory, the vent thrust is calculated using the isentropic and isothermal air depressurization models. Then derivations are shown for the estimations of vent thrust, attitude and vent torque. Finally numerical simulations for the leak localization are presented and an example of the shuttle airlock depressurization effect on the ISS is shown using actual data.

2. PRELIMINARIES

Spacecraft Attitude Kinematics

In this section the attitude kinematics and dynamics of the ISS in the presence of external disturbances in LEO are derived. For the attitude kinematics, the quaternion is used to specify the attitude of the ISS [9]. The quaternion is defined as

$$\mathbf{q} \equiv \begin{bmatrix} q_{13} \\ q_4 \end{bmatrix} \quad (1)$$

where the vector part \mathbf{q}_{13} is

$$\mathbf{q}_{13} \equiv \begin{bmatrix} q_1 \\ q_2 \\ q_3 \end{bmatrix} = \hat{\mathbf{n}} \sin\left(\frac{\theta}{2}\right) \quad (2)$$

and the scalar part q_4 is

$$q_4 = \cos\left(\frac{\theta}{2}\right) \quad (3)$$

where $\hat{\mathbf{n}}$ is a unit vector indicating the principal rotation axis and θ is the principal rotation angle. The quaternion components satisfy the following normalization constraint

$$\mathbf{q}^T \mathbf{q} = q_1^2 + q_2^2 + q_3^2 + q_4^2 = 1 \quad (4)$$

The quaternion kinematic equations of motion are given by

$$\dot{\mathbf{q}} = \frac{1}{2} \Omega(\boldsymbol{\omega}) \mathbf{q} \quad (5)$$

where $\boldsymbol{\omega}$ is the angular velocity and Ω is defined as

$$\Omega(\boldsymbol{\omega}) \equiv \begin{bmatrix} -[\boldsymbol{\omega} \times] & \vdots & \boldsymbol{\omega} \\ \dots & \dots & \dots \\ -\boldsymbol{\omega}^T & \vdots & 0 \end{bmatrix} \quad (6)$$

where $[\boldsymbol{\omega} \times]$ represents the skew-symmetric matrix, defined by

$$[\boldsymbol{\omega} \times] \equiv \begin{bmatrix} 0 & -\omega_3 & \omega_2 \\ \omega_3 & 0 & -\omega_1 \\ -\omega_2 & \omega_1 & 0 \end{bmatrix} \quad (7)$$

If the attitude quaternion \mathbf{q} represents the orientation of the body reference frame with respect to the Local-Vertical-Local-Horizontal (LVLH) orbital reference frame then the velocity vector $\boldsymbol{\omega} = \boldsymbol{\omega}_{B/L}$ is given by

$$\boldsymbol{\omega}_{B/L} = \boldsymbol{\omega}_{B/N} + n \mathbf{C}_2(\mathbf{q}) \quad (8)$$

where $\boldsymbol{\omega}_{B/N}$ is the angular velocity with respect to an inertial frame, \mathbf{C}_i is the i^{th} column of the coordinate transformation matrix from the LVLH orbital reference frame to the body reference frame, and n is the orbital frequency of the spacecraft [10].

Spacecraft Attitude Dynamics

The dynamic equations of rotational motion of a rigid spacecraft in a LEO environment are given by Euler's equation:

$$\dot{\mathbf{H}} = -[J^{-1}(\mathbf{H} - \mathbf{h})] \times \mathbf{H} + \mathbf{N}_{drag} + \mathbf{N}_{grav} + \mathbf{d}_{vent} \quad (9)$$

where \mathbf{H} is the total angular momentum of the spacecraft satisfying

$$\mathbf{H} = J\boldsymbol{\omega} + \mathbf{h} \quad (10)$$

and J is the inertia matrix, \mathbf{N}_{drag} is the aerodynamic torque, \mathbf{N}_{grav} is the gravity gradient torque, \mathbf{h} is the angular momentum of the control moment gyroscopes (CMGs), and \mathbf{d}_{vent} is

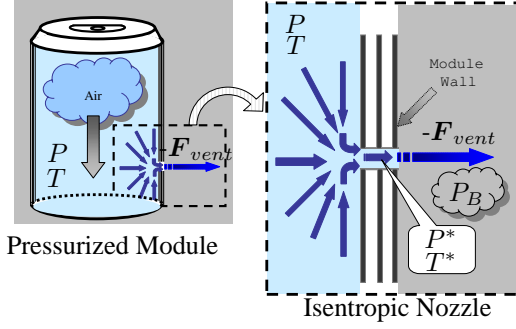


Figure 1. Air Flow Through Leak Hole

the torque due to a vent. Other environmental effects such as solar radiation and Earth's albedo are neglected. The effects caused by solar arrays rotations are omitted since they have little effects on the attitude dynamics but note that the resultant aerodynamic torques produced by the arrays rotations may be significant.

The gravity-gradient torque for a circular orbiting spacecraft is given by

$$\mathbf{N}_{grav} = 3n^2 \mathbf{C}_3(\mathbf{q}) \times \mathbf{J} \mathbf{C}_3(\mathbf{q}) \quad (11)$$

The aerodynamic torque \mathbf{N}_{drag} is modelled such that the drag force and the center of pressure location are functions of the attitude of the spacecraft:

$$\mathbf{N}_{drag} = -\frac{1}{2} \rho_a v_a^2 C_D S [\boldsymbol{\rho}_{cp} \times \mathbf{C}_1(\mathbf{q})] \quad (12)$$

where v_a is the magnitude of the atmospheric velocity with respect to the spacecraft, which can be approximated as the circular orbital speed. The atmospheric density ρ_a is calculated using Marshall Engineering Thermosphere (MET) model which accounts the seasonal and diurnal heating effects of the Earth's atmosphere. The drag coefficient C_D is assumed to be constant for a given orientation of the spacecraft. Also, S is the attitude dependent frontal area and $\boldsymbol{\rho}_{cp}$ is the attitude dependent center of pressure location. The attitude dependent aerodynamic parameters are calculated with the method developed in [10], where the reference area and the center of pressure are calculated for any orientation by defining interpolation functions. The projected area and the center of pressure for the three orthogonal body reference axes of the ISS are given in [1] for each assembly stage.

The vent torque is modelled by

$$\mathbf{d}_{vent} = \mathbf{r}_{vent} \times \mathbf{F}_{vent} \quad (13)$$

where \mathbf{r}_{vent} is the moment arm of a vent torque from the center of mass of the spacecraft to a leak location, and \mathbf{F}_{vent} is a vent thrust. The vent torque is unknown and will be estimated by treating it as a state in the real-time filter algorithm.

Vent Thrust

A leak hole perforated on the surface of a pressurized module will behave like a short length nozzle. The dynamic properties of the air flow through the leak hole are analyzed using one dimensional isentropic and isothermal nozzle dynamic models. Fig. 1 shows the diagram of the air flow through the leak hole on the pressurized module, where T^* and P^* are the temperature and pressure of the air in the leak hole, respectively, T and P are the temperature and pressure of the inside of the pressurized module, respectively, \mathbf{F}_{vent} is the vent thrust, and P_B is the back pressure. The mass flow rate in a leak hole is given by [11]

$$\dot{m} = -\frac{AP^*v^*}{RT^*} \quad (14)$$

where A is the area of the hole, R is the ideal gas constant (287 N-m/Kg-K), and v^* is the exhaust velocity of the air satisfying

$$v^* = \sqrt{\gamma RT^*} \quad (15)$$

where γ is the specific heat ratio, with $\gamma = 1.4$ for an ideal gas. The mass flow rate \dot{m} can be expressed as a function of the air inside the pressurized module. This is accomplished by substituting the following expressions into Eq. (14):

$$P^* = P \left(\frac{2}{\gamma + 1} \right)^{\frac{\gamma}{\gamma - 1}} \quad (16a)$$

$$T^* = T \left(\frac{2}{\gamma + 1} \right) \quad (16b)$$

yielding

$$\dot{m} = -\frac{AP\sqrt{\gamma}}{\sqrt{RT}} \left(\frac{2}{1 + \gamma} \right)^{\frac{1 + \gamma}{2(\gamma - 1)}} \quad (17)$$

The actual mass flow rate can be calculated by multiplying \dot{m} in Eq. (14) by the discharge coefficient C_D . Using the thrust equation the vent thrust magnitude is given by

$$|\mathbf{F}_{vent}| = C_D \dot{m} v^* + (P^* - P_a)A \quad (18)$$

where P_a is the ambient pressure which is approximately zero for the vacuum of space. Substituting Eqs. (14), (15) and (16) into Eq. (18), and simplifying yields

$$|\mathbf{F}_{vent}| = AP(C_D \gamma + 1) \left(\frac{2}{\gamma + 1} \right)^{\frac{\gamma}{\gamma - 1}} \quad (19)$$

Note that the magnitude of the vent thrust is proportional to the pressure inside the module and to the area of the leak hole. This expression is very useful since the vent thrust magnitude is a direct function of the internal pressure P , which can be measured by a pressure sensor. For the calculation of the hole area A the following approach is used. The indication of an air leak in a pressurized module is the depressurization of the air. The air inside the module follows the ideal gas law, given by

$$P = \frac{mRT}{V} \quad (20)$$

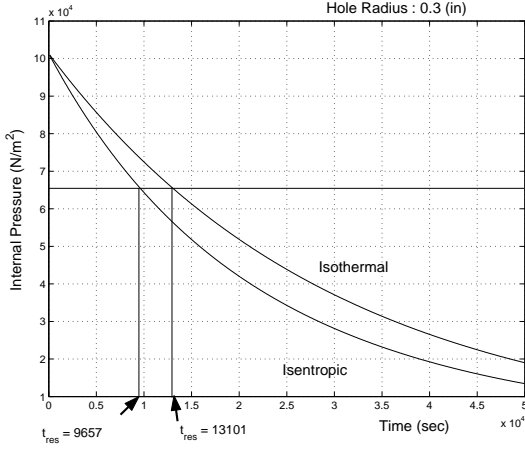


Figure 2. Internal Pressure

where V is the volume of the air. Differentiating Eq. (20) with respect to time and using \dot{m} from Eq. (17) gives a depressurization rate model. Two kinds of depressurization process models are used, depending on the temperature characteristics of the air. For an isentropic air model, where P and T is related by

$$T = T_0 \left(\frac{P}{P_0} \right)^{\frac{\gamma-1}{\gamma}} \quad (21)$$

the depressurization rate \dot{P} is

$$\dot{P} = -k_1 A P^{k_2} \quad (22a)$$

$$k_1 = \frac{\gamma \sqrt{RT_0 \gamma}}{V} P_0^{\frac{1-\gamma}{2\gamma}} \left(\frac{2}{\gamma+1} \right)^{\frac{\gamma+1}{2(\gamma-1)}} C_D \quad (22b)$$

$$k_2 = \frac{3\gamma-1}{2\gamma} \quad (22c)$$

For an isothermal process, T is treated as a constant in Eq. (20). Therefore the depressurization rate \dot{P} can be derived as

$$\dot{P} = -k_3 A P_0 \quad (23a)$$

$$k_3 = \frac{\sqrt{RT_0 \gamma}}{V} \left(\frac{2}{1+\gamma} \right)^{\frac{1+\gamma}{2(\gamma-1)}} C_D \quad (23b)$$

where the subscript 0 stands for the initial value and, k_1 , k_2 and k_3 are constants. Now, we can calculate the hole area A by measuring the internal pressure P and its depress rate \dot{P} .

Comparisons between the isentropic and isothermal gas model are shown in Figs. 2 and 3, using the ISS assembly Stage 16A with a leak hole radius of 0.3 inch. From Fig. 2, the isentropic gas model gives a faster pressure drop in the internal pressure than the isothermal gas model. Therefore the reserve time t_{res} , which is a measure of the time it takes for the current pressure P to reach the minimum habitable pressure $P_{min} \approx 490$ mmHg, is shorter using the isentropic gas model than using the isothermal gas model. The reserve time

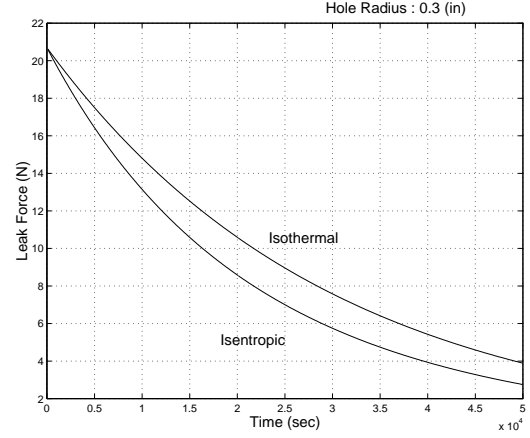


Figure 3. Vent Thrust Magnitude

t_{res} can be obtained by integrating Eq. (22b) for the isentropic process and Eq. (23a) for the isothermal process. The reserve time for the isentropic process is

$$t_{res} = \frac{\left(\frac{P_{min}}{P} \right)^{\frac{1-\gamma}{2\gamma}} - 1}{\frac{\gamma-1}{2} \frac{A}{V} \sqrt{RT\gamma} \left(\frac{2}{\gamma+1} \right)^{\frac{\gamma+1}{2(\gamma-1)}} C_D} \quad (24)$$

where the internal temperature T can be substituted by P from Eq. (21). From Fig. 3 the vent thrust magnitude is larger using the isothermal gas model, meaning the isothermal gas model produces a greater torque than the isentropic gas model. If the leak area hole size is small then the isothermal model can be used (since the temperature will remain fairly constant), otherwise the isentropic model should be used.

3. ESTIMATION OF VENT THRUST MAGNITUDE

Since the actual internal pressure measurements are corrupted by noise, the Kalman filter is used to estimate the hole area which is needed to calculate the magnitude of vent thrust with Eq. (19). The state equations for the depressurization process have the following form

$$\dot{\mathbf{x}}(t) = \mathbf{f}[\mathbf{x}(t), t] + \boldsymbol{\eta}(t) \quad (25)$$

where the state $\mathbf{x}(t) = [P(t), A(t)]^T$ and

$$\mathbf{f}[\mathbf{x}(t), t] = \begin{bmatrix} -k_1 A P^{k_2} \\ 0 \end{bmatrix} \quad (26)$$

for an isentropic process model, and

$$\mathbf{f}[\mathbf{x}(t), t] = \begin{bmatrix} -k_3 A P \\ 0 \end{bmatrix} \quad (27)$$

for isothermal process model. The vector $\boldsymbol{\eta} = [\eta_1, \eta_2]^T$ is the process noise vector, where η_1 and η_2 are Gaussian white-noise processes with

$$E\{\eta_i(t)\} = 0 \quad (28a)$$

$$E\{\eta_i(t)\eta_j(t')\} = Q_i \delta_{i,j}(t-t') \quad (28b)$$

with $i, j = 1, 2$. The matrix Q_i has the following form

$$Q = \begin{bmatrix} \sigma_1^2 & 0 \\ 0 & \sigma_2^2 \end{bmatrix} \quad (29)$$

where the terms σ_1^2 and σ_2^2 are the variances of η_1 and η_2 , respectively. The internal pressure measurement is modelled as

$$\tilde{z}_k = h_k[\mathbf{x}(t_k)] + v_k, \quad k = 1, 2, \dots, m \quad (30a)$$

$$h_k[\mathbf{x}(t_k)] = P_k, \quad k = 1, 2, \dots, m \quad (30b)$$

where m is the number of measurements and v_k is the measurement noise which satisfies a discrete Gaussian white-noise process with

$$E\{v_k\} = 0 \quad (31a)$$

$$E\{v_k v_{k'}\} = R_k \delta_{k,k'} \quad (31b)$$

The propagation of the state satisfies

$$\dot{\hat{\mathbf{x}}}(t) = \mathbf{f}[\hat{\mathbf{x}}(t), t] \quad (32a)$$

$$\hat{z}_k = h_k[\hat{\mathbf{x}}(t_k)] \quad (32b)$$

where $\hat{\mathbf{x}}(t) = [\hat{P}(t), \hat{A}(t)]^T$ is the state estimate vector. The error covariance propagation matrix \mathcal{P} satisfies

$$\dot{\mathcal{P}}(t) = F[\hat{\mathbf{x}}(t), t] \mathcal{P}(t) + \mathcal{P}(t) F[\hat{\mathbf{x}}(t), t]^T + Q \quad (33)$$

where $F[\hat{\mathbf{x}}(t), t]$ is given by

$$F[\hat{\mathbf{x}}(t), t] = \left. \frac{\partial \mathbf{f}[\mathbf{x}(t), t]}{\partial \mathbf{x}(t)} \right|_{\mathbf{x}=\hat{\mathbf{x}}} \quad (34a)$$

$$= \begin{bmatrix} -k_1 k_2 \hat{P}^{k_2-1} & -k_1 \hat{P}^{k_2} \\ 0 & 0 \end{bmatrix} \quad (34b)$$

for an isentropic process, and

$$F[\hat{\mathbf{x}}(t), t] = \left. \frac{\partial \mathbf{f}[\mathbf{x}(t), t]}{\partial \mathbf{x}(t)} \right|_{\mathbf{x}=\hat{\mathbf{x}}} \quad (35a)$$

$$= \begin{bmatrix} -k_3 \hat{A} & -k_1 \hat{P} \\ 0 & 0 \end{bmatrix} \quad (35b)$$

for an isothermal process.

The state estimate and error covariance updates are given by

$$\hat{\mathbf{x}}_k^+ = \hat{\mathbf{x}}_k^- + K_k [\tilde{z}_k - h_k(\hat{\mathbf{x}}_k^-)] \quad (36a)$$

$$\mathcal{P}_k^+ = [I - K_k H_k(\hat{\mathbf{x}}_k^-)] \mathcal{P}_k^- \quad (36b)$$

where the superscript (+) stands for the updated value and (-) stands for the a priori value. The Kalman gain matrix is given by

$$K_k = \mathcal{P}_k^- H_k(\hat{\mathbf{x}}_k^-)^T [H_k(\hat{\mathbf{x}}_k^-) \mathcal{P}_k^- H_k(\hat{\mathbf{x}}_k^-)^T + R_k]^{-1} \quad (37)$$

where $H_k(\hat{\mathbf{x}}_k^-)$ is the measurement sensitivity matrix, given by

$$H_k(\hat{\mathbf{x}}_k^-) = \left. \frac{\partial h_k(\mathbf{x}(t_k))}{\partial \mathbf{x}(t_k)} \right|_{\mathbf{x}=\hat{\mathbf{x}}} \quad (38)$$

$$= [1 \quad 0]$$

Thus with the use of the internal pressure measurements the EKF algorithm can be used to estimate the leak hole area. Then the magnitude of vent thrust can be calculated by substituting the estimated values of \hat{P} and \hat{A} into Eq. (19).

4. UNSCENTED FILTER

An unscented filtering approach is considered here as an alternative to the EKF for the attitude and angular rate estimation of the ISS. The Unscented Filter (UF) has first been proposed by Julier and Uhlman in [3]. Unlike the EKF, the UF captures the posterior mean and covariance of a random variable accurately to the second-order Taylor series expansion for any nonlinearity by choosing a minimal set of sample points and propagating them through the original nonlinear system. Also it is derivative-free, i.e. no Jacobian and Hessian calculations need to be evaluated for the computation. Therefore it can be easily applied to any complex dynamical system and to non-differentiable functions [5]. A detailed description of the error performance of the UF over EKF can be found in Refs. [3], [5] and [12]. The general formulation of the UF in discrete-time is described here.

Let the discrete-time nonlinear system and observation model be

$$\mathbf{x}_{k+1} = \mathbf{f}(\mathbf{x}_k, \mathbf{u}_k, k) + \mathbf{w}_k \quad (39a)$$

$$\tilde{\mathbf{y}}_{k+1} = \mathbf{h}(\mathbf{x}_{k+1}, \mathbf{u}_{k+1}, k+1) + \mathbf{v}_{k+1} \quad (39b)$$

where \mathbf{x}_{k+1} and \mathbf{y}_{k+1} is an n dimensional state vector and observation vector respectively, \mathbf{f} and \mathbf{h} are the nonlinear models, \mathbf{u}_k is a deterministic input, and \mathbf{w}_k and \mathbf{v}_{k+1} are zero mean Gaussian process and measurement noise, respectively. The process noise \mathbf{w}_k and measurement noise \mathbf{v}_k are assumed to be uncorrelated with covariances

$$E[\mathbf{w}_i \mathbf{w}_j^T] = \delta_{ij} Q(j) \quad (40a)$$

$$E[\mathbf{v}_i \mathbf{v}_j^T] = \delta_{ij} R(j) \quad (40b)$$

$$E[\mathbf{w}_i \mathbf{v}_j^T] = \mathbf{0}, \forall i, j \quad (40c)$$

Note that using a numerical integration scheme, a continuous system model can always be expressed in the discrete form equations. In the EKF, problems arise because the predictions are approximated simply as functions of the previous state estimates:

$$\hat{\mathbf{x}}_{k+1}^- = E[\mathbf{f}(\mathbf{x}_k, \mathbf{u}_k, k)] \approx \mathbf{f}(\hat{\mathbf{x}}_k, \mathbf{u}_k, k) \quad (41)$$

$$\hat{\mathbf{y}}_{k+1}^- = E[\mathbf{h}(\mathbf{x}_k, \mathbf{u}_k, k)] \approx \mathbf{h}(\hat{\mathbf{x}}_k, \mathbf{u}_k, k) \quad (42)$$

But if the estimated state is nearby the true value, then the filter usually has a good convergence.

The UF state and error covariance updates are given as

$$\hat{\mathbf{x}}_k^+ = \hat{\mathbf{x}}_k^- + K_k \mathbf{v}_k \quad (43)$$

$$\mathbf{v}_k = \tilde{\mathbf{y}}_k - \hat{\mathbf{y}}_k^- = \tilde{\mathbf{y}}_k - \mathbf{h}(\hat{\mathbf{x}}_k^-, \mathbf{u}_k, k) \quad (44)$$

$$P_k^+ = P_k^- - K_k P_k^{vv} K_k^T \quad (45)$$

$$K_k = P_k^{xy} (P_k^{vv})^{-1} \quad (46)$$

where \mathbf{v}_k is the innovation and P_k^{vv} is the covariance of \mathbf{v}_k . The filter gain is K_k and P_k^{xy} is the cross-correlation matrix between $\hat{\mathbf{x}}_k^-$ and $\hat{\mathbf{y}}_k^-$. The set of $2n$ σ -points are computed as follows:

$$\sigma_k(i) = \pm \sqrt{(n+\lambda)[P_k + Q_k]_i} \quad \text{where } i = 1, 2, \dots, n \quad (47)$$

where λ is the weighting factor which scales the distribution of the points. The vector $\sqrt{(n+\lambda)[P_k + Q_k]_i}$ represents i^{th} column of the matrix square-root $\sqrt{(n+\lambda)[P_k + Q_k]}$. The matrix square-root can be calculated directly by a lower triangular Cholesky factorization method.

These $\sigma_k(i)$ points translate the mean $\hat{\mathbf{x}}_k^+$ as

$$\chi(0) = \hat{\mathbf{x}}_k^+, \quad \chi(i) = \hat{\mathbf{x}}_k^+ + \sigma_k(i) \quad (48)$$

The transformed set of χ points are propagated to $k+1$ for each of the $2n+1$ points by

$$\begin{aligned} \chi_{k+1}(0) &= \mathbf{f}(\chi_k(0), \mathbf{u}_k, k) \\ \chi_{k+1}(i) &= \mathbf{f}(\chi_k(i), \mathbf{u}_k, k) \end{aligned} \quad (49)$$

The predicted mean is

$$\hat{\mathbf{x}}_{k+1}^- = \frac{1}{n+\lambda} \left\{ \lambda \chi_{k+1}(0) + \frac{1}{2} \sum_{i=1}^{2n} \chi_{k+1}(i) \right\} \quad (50)$$

and the predicted covariance is

$$\begin{aligned} P_{k+1}^- &= \frac{1}{n+\lambda} \left\{ \lambda [\chi_{k+1}(0) - \hat{\mathbf{x}}_{k+1}^-] [\chi_{k+1}(0) - \hat{\mathbf{x}}_{k+1}^-]^T \right. \\ &\quad \left. + \frac{1}{2} \sum_{i=1}^{2n} [\chi_{k+1}(i) - \hat{\mathbf{x}}_{k+1}^-] [\chi_{k+1}(i) - \hat{\mathbf{x}}_{k+1}^-]^T \right\} \end{aligned} \quad (51)$$

The predicted observation is calculated as

$$\hat{\mathbf{y}}_{k+1}^- = \frac{1}{n+\lambda} \left\{ \lambda \gamma_{k+1}(0) + \frac{1}{2} \sum_{i=1}^{2n} \gamma_{k+1}(i) \right\} \quad (52)$$

where

$$\gamma_{k+1}(i) = \mathbf{h}(\chi_{k+1}(i), \mathbf{u}_{k+1}, k+1) \quad (53)$$

The output covariance is given by

$$\begin{aligned} P_{k+1}^{yy} &= \frac{1}{n+\lambda} \left\{ \lambda [\gamma_{k+1}(0) - \hat{\mathbf{y}}_{k+1}^-] [\gamma_{k+1}(0) - \hat{\mathbf{y}}_{k+1}^-]^T \right. \\ &\quad \left. + \frac{1}{2} \sum_{i=1}^{2n} [\gamma_{k+1}(i) - \hat{\mathbf{y}}_{k+1}^-] [\gamma_{k+1}(i) - \hat{\mathbf{y}}_{k+1}^-]^T \right\} \end{aligned} \quad (54)$$

then the innovation covariance is given by

$$P_{k+1}^{vv} = P_{k+1}^{yy} + R_{k+1} \quad (55)$$

Finally the cross correlation matrix is

$$\begin{aligned} P_{k+1}^{xy} &= \frac{1}{n+\lambda} \left\{ \lambda [\chi_{k+1}(0) - \hat{\mathbf{x}}_{k+1}^-] [\gamma_{k+1}(0) - \hat{\mathbf{y}}_{k+1}^-]^T \right. \\ &\quad \left. + \frac{1}{2} \sum_{i=1}^{2n} [\chi_{k+1}(i) - \hat{\mathbf{x}}_{k+1}^-] [\gamma_{k+1}(i) - \hat{\mathbf{y}}_{k+1}^-]^T \right\} \end{aligned} \quad (56)$$

The filter gain, the state and error covariance update is then computed using Eqs. (43) and (46). The weight λ can be chosen as $\lambda = 3 - n$ if the state \mathbf{x} is assumed to belong to the Gaussian distribution [13]. Although λ can be either positive or negative, negative values may lead to a nonpositive semi-definite covariance matrix. In this case a modified form of the state covariance can be used [12], given by

$$\begin{aligned} P_{k+1}^- &= \frac{1}{2(n+\lambda)} \sum_{i=1}^{2n} [\chi_{k+1}(i) - \hat{\mathbf{x}}_{k+1}^-] \\ &\quad \times [\chi_{k+1}(i) - \hat{\mathbf{x}}_{k+1}^-]^T \end{aligned} \quad (57)$$

Note that in higher-order systems the computational load of the UF may be comparable to that of the EKF (especially if complex Jacobian computations need to be performed) but studies to date [4], [5], [12] and [13] indicate we can expect an improved filter performance.

Attitude Estimation Using USQUE Approach

The main topic in this section is a new attitude filtering approach called the Unscented Quaternion Estimator (USQUE) developed by Crassidis and Markley [4]. Many of the conventional attitude estimation methods process the attitude sensor data by employing the EKF method (see [14]). In the method derived in Ref. [14], the attitude propagation is done by using the attitude and the angular rate data from the gyros measurement. The biases in the gyroscopes are estimated during the attitude filtering process by treating them as augmented filter states. However the angular rate is not treated as a filter state but the angular rate measurement noise appears as a process noise in the filter equations. This approach avoids the use of the complex attitude dynamics, which may be subject to large uncertainties. The attitude is represented using a singularity-free quaternion whose kinematics equation has a bilinear form. But a singularity arises in the filter covariance matrix because the four components of the quaternion satisfy the normalization constraint. To avoid the difficulty of numerically maintaining this singularity, the four components of the quaternion are replaced by three-component error vector for the state error covariance propagation. This approach has a good convergence when the true attitude trajectory is near the estimate state since it uses the linearized attitude kinematics equation.

On the other hand, the USQUE algorithm does not need any linearization procedure when deriving the filter equations

since the state undergoes the unscented transform process (see [13]). But this algorithm is not directly suited to be used with the quaternion since its estimated value is derived using an average sum of the quaternions. Instead, a modified method employing the combination of the quaternion with the generalized Rodrigues parameters is used [4]. This attitude estimation method uses the inertial quaternion for the state propagation and employs the generalized Rodrigues parameters to calculate the mean, the state error covariance and the cross-correlation matrix with a vector output sensor measurement. This algorithm is modified in this paper to incorporate the sensor output measurement represented by the quaternion which represents the orientation of the body frame with respect to LVLH frame. A comparison of the USQUE and the conventional method [14] will be discussed at the end by showing numerical simulation results. The USQUE algorithm derivation explained here is based on Ref. [4].

The attitude kinematics of the ISS can be expressed in terms of the quaternion by substituting Eqs. (5) into (8) giving

$$\dot{\mathbf{q}} = \frac{1}{2}\Omega(\boldsymbol{\omega}_{B/N} + n\mathbf{C}_2(\mathbf{q}))\mathbf{q} \quad (58)$$

where \mathbf{q} is the attitude quaternion expressing the orientation of the body frame with respect to the orbital LVLH frame. For notational convenience let us define the angular rate of the body frame with respect to LVLH as $\boldsymbol{\omega} = \boldsymbol{\omega}_{B/N} + n\mathbf{C}_2(\mathbf{q})$. But note that the circular orbital frequency, n , is a well-known quantity which can be easily calculated for a circular orbit. The error quaternion in this paper is defined as [14]

$$\delta\mathbf{q} \equiv \mathbf{q} \otimes \hat{\mathbf{q}}^{-1} = C(\mathbf{q})C(\hat{\mathbf{q}}^{-1}) \quad (59)$$

where C is the direction cosine matrix and $\hat{\mathbf{q}}^{-1}$ is the inverse quaternion of the estimated values defined as

$$\hat{\mathbf{q}}^{-1} \equiv \begin{bmatrix} -\hat{q}_{13} \\ \hat{q}_4 \end{bmatrix} \quad (60)$$

The error quaternion can be represented by [4]

$$\delta\mathbf{p} \equiv f \frac{\delta\mathbf{q}_{13}}{a + \delta q_4} \quad (61)$$

where $\delta\mathbf{p}$ is a generalized Rodrigues parameters [15], $\delta\mathbf{q}_{13}$ and δq_4 are the vector part and scalar part of $\delta\mathbf{q}$, respectively, a is a parameter from 0 to 1, and f is a scale factor. Note that for a Gibbs vector, $a = 0$ and $f = 1$, but when $f = 2(a + 1)$, $\|\mathbf{p}\|$ is equal to the rotational angle about the Euler axis. The inverse transform from \mathbf{p} to \mathbf{q} can be written as [4]

$$\delta q_4 = \frac{-a\|\delta\mathbf{p}\|^2 + f\sqrt{f^2 + (1 - a^2)\|\delta\mathbf{p}\|^2}}{f^2 + \|\delta\mathbf{p}\|^2} \quad (62a)$$

$$\delta\mathbf{q}_{13} = f^{-1}(a + \delta q_4)\delta\mathbf{p} \quad (62b)$$

The sensor output measurement model is given by

$$\tilde{\mathbf{y}}(k + 1) = \delta\mathbf{q}_v(k + 1) \otimes \mathbf{q}(k + 1) \quad (63)$$

where $\delta\mathbf{q}_v(k + 1)$ is the unit quaternion which represents a perturbation in attitude corresponding to the Gaussian sensor noise satisfying Eq. (40b).

The gyroscope measurement output $\tilde{\boldsymbol{\omega}}$ is modeled as [16]

$$\tilde{\boldsymbol{\omega}} = \boldsymbol{\omega} + \mathbf{b} + \boldsymbol{\eta}_1 \quad (64a)$$

$$\dot{\mathbf{b}} = \boldsymbol{\eta}_2 \quad (64b)$$

where $\boldsymbol{\omega}$ is the true spacecraft angular rate, $\boldsymbol{\eta}_1$ and $\boldsymbol{\eta}_2$ are zero-mean Gaussian white-noise process and \mathbf{b} is a gyro bias error. The post-update estimates of $\boldsymbol{\omega}$ and \mathbf{b} are given by

$$\hat{\boldsymbol{\omega}}_k^+ = \tilde{\boldsymbol{\omega}} - \mathbf{b}_k^+ \quad (65a)$$

$$\mathbf{b}_{k+1}^- = \mathbf{b}_k^+ \quad (65b)$$

The quaternion can then be propagated in discrete-form with [4]

$$\hat{\mathbf{q}}_{k+1}^- = \Omega(\hat{\boldsymbol{\omega}}_k^+) \hat{\mathbf{q}}_k^+ \quad (66)$$

where

$$\Omega(\hat{\boldsymbol{\omega}}_k^+) \equiv \begin{bmatrix} \cos(0.5\|\hat{\boldsymbol{\omega}}_k^+\|\Delta t)I_{3 \times 3} - [\hat{\boldsymbol{\psi}}_k^+ \times] & \hat{\boldsymbol{\psi}}_k^+ \\ -\hat{\boldsymbol{\psi}}_k^{+T} & \cos(0.5\|\hat{\boldsymbol{\omega}}_k^+\|\Delta t) \end{bmatrix} \quad (67)$$

where $\hat{\boldsymbol{\psi}}_k^+ = \sin(0.5\|\hat{\boldsymbol{\omega}}_k^+\|\Delta t)\hat{\boldsymbol{\omega}}_k^+/\|\hat{\boldsymbol{\omega}}_k^+\|$ and Δt is the sampling interval of the gyro measurement.

In the USQUE algorithm, the state is defined as

$$\hat{\mathbf{x}}_k^+ = \boldsymbol{\chi}_k(0) \equiv \begin{bmatrix} \delta\hat{\mathbf{p}}_k^+ \\ \hat{\mathbf{b}}_k^+ \end{bmatrix} \quad (68)$$

Therefore, a 3-dimensional attitude representation is possible making the 6-dimensional covariance matrix nonsingular. The 12 σ -points can be calculated using Eq. (47) with $\lambda = -3$ since the six-component state errors are assumed to follow the Gaussian distribution. Then by adding these 12 σ -points to the mean value obtained in Eq. (68) gives the 12 translated $\boldsymbol{\chi}_k(i)$ points around the mean value (see Eq. (48)), yielding

$$\boldsymbol{\chi}_k(i) \equiv \begin{bmatrix} \boldsymbol{\chi}_k^p(i) \\ \boldsymbol{\chi}_k^b(i) \end{bmatrix} \quad \text{where } i = 0, 1, 2, \dots, 12 \quad (69)$$

where $\boldsymbol{\chi}_k^p$ and $\boldsymbol{\chi}_k^b$ are the Rodrigues and gyro bias part of the state vector, respectively. Note that the mean value is also included in Eq. (69). These scattered points are then converted to an error quaternion for the propagation to $k + 1$. The conversion of from the $\boldsymbol{\chi}_k(i)$ points to the error quaternion is done using Eq. (62a) and (62b) for each $\boldsymbol{\chi}_k^p$ point. Then the resulting 13 error quaternions are converted to the current quaternion estimates by

$$\hat{\mathbf{q}}_k^+(0) = \hat{\mathbf{q}}_k^+ \quad (70a)$$

$$\hat{\mathbf{q}}_k^+(i) = \delta\mathbf{q}_k^+(i) \otimes \hat{\mathbf{q}}_k^+ \quad \text{where } i = 1, 2, \dots, 12 \quad (70b)$$

Then these quaternions are propagated to $k + 1$ using Eq. (71) as

$$\hat{\mathbf{q}}_{k+1}^- (i) = \Omega (\hat{\omega}_k^+ (i)) \hat{\mathbf{q}}_k^+ (i) \quad (71)$$

where the estimated angular rate satisfies

$$\hat{\omega}_k^+ (i) = \tilde{\omega}_k - \mathbf{b}_k^+ (i) \quad \text{where } i = 0, 1, \dots, 12 \quad (72)$$

The reason why $\delta \mathbf{p}$ is not propagated directly using its kinematic equation is that the quaternion kinematics equation has a closed-form solution, as given in Eq. (71), and also it is computationally more efficient [4]. Then at $k + 1$ the propagated quaternion is reconverted to a error quaternion using

$$\delta \mathbf{q}_{k+1}^- (i) = \hat{\mathbf{q}}_{k+1}^- (i) \otimes [\hat{\mathbf{q}}_{k+1}^- (0)]^{-1} \quad \text{where } i = 0, 1, \dots, 12 \quad (73)$$

Next, the 13 $\chi_{k+1}^p (i)$ points are again calculated by converting the error quaternion into $\delta \mathbf{p}$, and then the state covariance is calculated using Eq. (51). Since the measurement is a quaternion, the mean of the observation at $k + 1$ is calculated again by the Rodrigues parameters as was done for the calculation of the mean attitude state. For this purpose, the following output error quaternion should be calculated first:

$$\delta \mathbf{q}_{k+1} = \tilde{\mathbf{q}}_{k+1} \otimes [\hat{\mathbf{q}}_{k+1}^- (0)]^{-1} \quad (74)$$

Then $\delta \mathbf{q}_{k+1}$ is converted to a Rodrigues parameter and the output and the cross-correlation covariance are calculated using Eqs. (54) and (56). The filter gain is obtained using Eq. (46).

For the calculation of the discrete process noise matrix Q_k in Eq. (47), an expression for the $\delta \mathbf{p}(t)$ propagation equation is needed, although the quaternion is propagated instead. From Refs. [4] and [17], the propagation for the $\delta \mathbf{p}(t)$ when $f = 2(a + 1)$ can be expressed approximately as

$$\begin{aligned} \delta \dot{\mathbf{p}}(t) = & -\hat{\omega}(t) \times \delta \mathbf{p}(t) + \delta \omega(t) - \frac{1}{2} \delta \omega(t) \times \delta \mathbf{p}(t) \\ & + \frac{1}{2f} [\delta \omega(t) \cdot \delta \mathbf{p}(t)] \delta \mathbf{p}(t) + \left(\frac{1}{4f} - \frac{1}{8} \right) [\delta \mathbf{p}(t) \cdot \delta \mathbf{p}(t)] \delta \omega(t) \end{aligned} \quad (75)$$

Then after some manipulations, the discrete covariance matrix Q_k can be obtained [4]

$$Q_k = \frac{\Delta t}{2} \begin{bmatrix} (\sigma_1^2 - \frac{1}{6} \sigma_2^2 \Delta t^2) I_{3 \times 3} & 0_{3 \times 3} \\ 0_{3 \times 3} & \sigma_2^2 I_{3 \times 3} \end{bmatrix} \quad (76)$$

where σ_1^2 and σ_2^2 are the power spectral density of the noise covariance $\boldsymbol{\eta}_1$ and $\boldsymbol{\eta}_2$, respectively.

Computer simulations for both USQUE and EKF are performed. The simulation parameters of the attitude sensor noise standard deviation is 0.5° , the gyroscope true rate bias is $[2.0626, 4.1253, 6.1879]^T$ $^\circ/\text{hr}$, the gyro rate output standard deviation is 2.3×10^{-4} $^\circ/\text{sec}$, measurement sampling rate of 1 Hz, and a small initial attitude estimate error and initial bias estimate of $0^\circ/\text{hr}$ for each axis. Note that the true

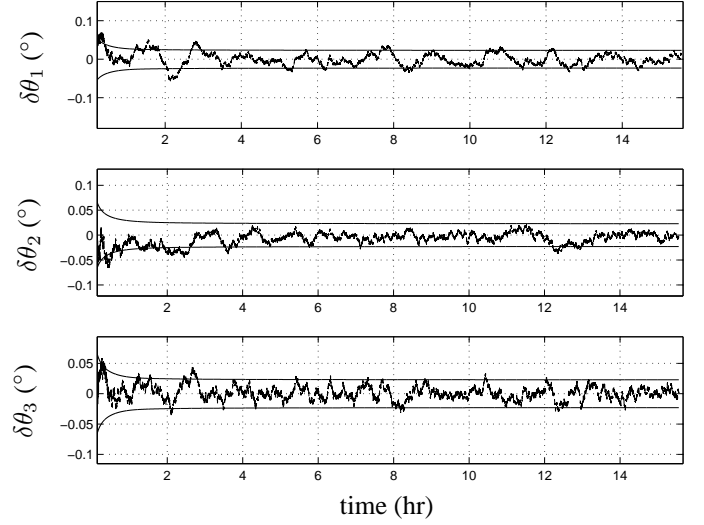


Figure 4. Attitude Estimation Error with 3σ Bounds

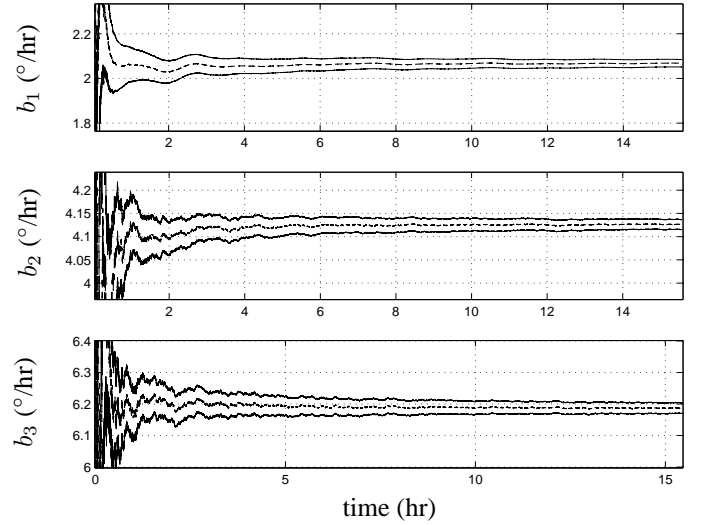


Figure 5. Bias Estimation with 3σ Bounds

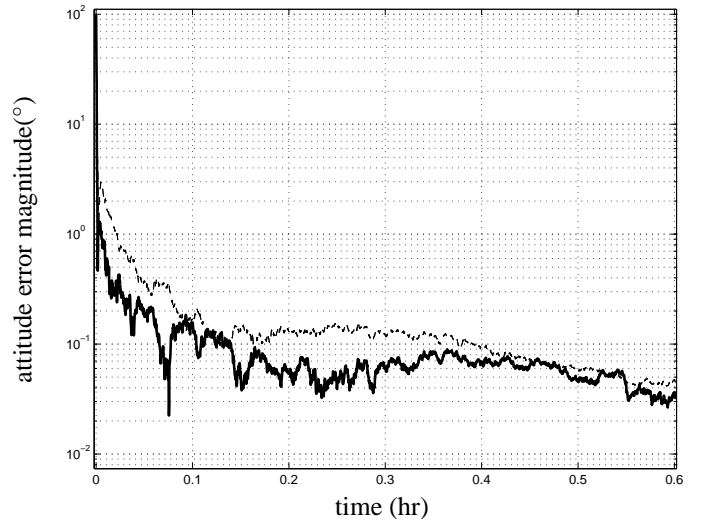


Figure 6. UF and EKF Attitude Estimation Errors

rate bias assumed in this simulation is not equivalent to that of the actual gyroscopes mounted on the ISS, but is chosen only to illustrate the performance of the USQUE algorithm. The USQUE attitude estimation errors for roll, pitch and yaw are shown in Fig. 4 with their $3\text{-}\sigma$ error bounds. We can see from the figure that the attitude estimates are within 0.5° for roll, pitch and yaw of their true values. In Fig. 5, the bias estimates using USQUE are plotted with their $3\text{-}\sigma$ confidence bounds. The superior performance of USQUE over the conventional EKF approach is not so obvious when the initial attitude estimate error is small (both filters have equivalent performances). But if there is large uncertainties in the initial estimates then the USQUE algorithm yields much better results compared to the conventional EKF method as shown in Fig. 6, where the initial attitude errors of 90° are used for each axis with the same rate bias as the previous case (values corresponding to the USQUE algorithm is plotted in wider solid line). We can see that the USQUE algorithm converges faster than the EKF method. Therefore in the presence of large uncertainties in the initial conditions, the USQUE algorithm is more optimal than the conventional EKF approach.

Residual Disturbance Torque Estimation

The vent torque, which is not explicitly modeled in the attitude dynamics, shows up as a residual disturbance torque when the spacecraft angular rate measurement undergoes a filtering process. In the disturbance torque estimation algorithm, the filter state vector is augmented to include the unknown parameters as additional states, resulting in a total of 6 filter states, where 3 states are for the angular rate or angular momentum of the spacecraft and the rest 3 states are for the 3-axis components of the disturbance torque. Note that the attitude quaternion, which is needed to determine the gravity-gradient and aerodynamic torque in the disturbance torque estimation algorithm, is estimated separately by the USQUE method described in the previous subsection. In this subsection the disturbance estimation algorithm using the UF approach is shown.

The state system model for the torque estimation filter with $\mathbf{x} = [\mathbf{H}, \mathbf{d}_{vent}]^T$ can be expressed as

$$\begin{aligned} \begin{bmatrix} \dot{\mathbf{H}} \\ \dot{\mathbf{d}}_{vent} \end{bmatrix} &= \begin{bmatrix} \mathbf{f}_H(\mathbf{H}, \mathbf{d}_{vent}) \\ \mathbf{f}_d(\mathbf{H}, \mathbf{d}_{vent}) \end{bmatrix} + \begin{bmatrix} \boldsymbol{\eta}_H \\ \boldsymbol{\eta}_d \end{bmatrix} \\ &= \begin{bmatrix} -\mathbf{J}^{-1}(\mathbf{H} - \mathbf{h}) \times \mathbf{H} + \mathbf{L} + \mathbf{d}_{vent} \\ \mathbf{0}_{3 \times 1} \end{bmatrix} + \begin{bmatrix} \boldsymbol{\eta}_H \\ \boldsymbol{\eta}_d \end{bmatrix} \end{aligned} \quad (77)$$

where \mathbf{d}_{vent} is the vent disturbance torque, $\boldsymbol{\eta}_H$ and $\boldsymbol{\eta}_d$ are zero-mean Gaussian process noises which correspond roughly to the possible range of the disturbance variations. The quantity \mathbf{L} is the external disturbance torque vector which can be expressed as

$$\mathbf{L} = \mathbf{N}_{drag} + \mathbf{N}_{grav} \quad (78)$$

The quantity \mathbf{L} is treated as a deterministic input in the filter equations. Also the CMG control input \mathbf{h} should be low pass

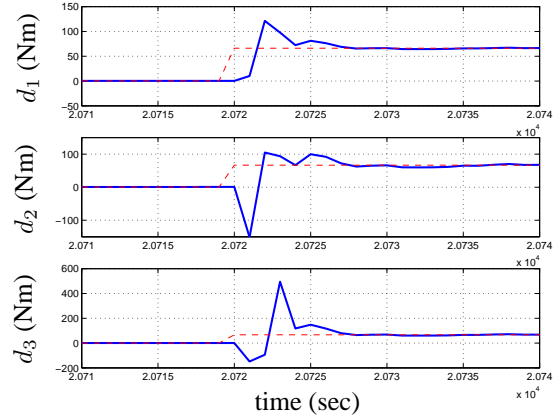


Figure 7. Vent Torque Estimate Using UF with True Value

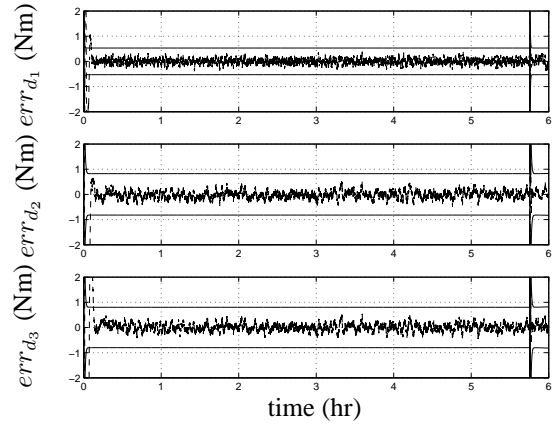


Figure 8. Disturbance Torque Estimation Error Using UF

filtered because of the presence of high-frequency noise when measuring the CMG wheel speed. Note that the vent torque \mathbf{d}_{vent} is treated as a random walk process. The gyroscope output measurement model is

$$\begin{aligned} \tilde{\mathbf{y}} &= \boldsymbol{\omega} + \boldsymbol{\eta}_1 \\ &= \mathbf{J}^{-1}(\mathbf{H} - \mathbf{h}) + \boldsymbol{\eta}_1 \end{aligned} \quad (79)$$

Unlike the EKF, the UF approach does not need any derivation of the Jacobian and the sensitivity matrices. For the UF we need only the original nonlinear equation and measurement model. In the disturbance estimation algorithm, the UF approach may be especially more robust than the EKF because the initial conditions for the angular rate components may be fairly accurate within the uncertainties of the gyroscope, but the initial guess of the disturbance torque, which is not measured, may be far from the true value.

Numerical simulations for the UF cases are performed with the angular rate noise standard deviation of 2.3×10^{-4} °/sec ($\sigma_1 = 4 \times 10^{-6}$ rad/sec) and the sampling frequency of 1 Hz for the ISS assembly stage UF1. It is assumed that the spacecraft attitude is maintaining the TEA when suddenly after 5.7556 hr (20720 sec) a vent torque of 66.07 Nm is applied

in each body axis of the spacecraft. The disturbance torque estimate results after the vent are shown in Fig. 7, where the dashed lines correspond to the true values. We can see that the vent torque estimates converge to the true values around 10 seconds after the leak. When an air leak occurs, the state covariance of the filter is reset to a large value to incorporate the variation of the disturbance torque at the instant when leak occurs (remember that we know when leak occurs by sensing the air depress inside the crew cabin). In this way the filter converges much faster than that of the filter algorithm without a covariance reset. The estimation errors for each component of the disturbance torque are shown in Fig. 8 with their 3σ -bound lines.

5. PARAMETER ESTIMATION

Parameter estimation is a process of extracting information about a system from measured input and output data. For the ISS, the uncertainty in the aerodynamic torque may affect the vent torque estimation results if they have the same order of magnitude. Also, uncertainties in the inertia matrix components may contribute to the residual disturbance to a certain degree when the spacecraft attitude is under acceleration due to a large vent torque. For the ISS, the inertia parameters for each configuration is pre-calculated on the ground with CAD tools. But these values may not be precise since the ISS is made up of multiple rigid bodies interconnected to each other and undergoes several configuration changes during its lifetime. Also the calculated atmosphere density with MET model has uncertainty of 15% (standard deviation) [18]. Although the center of pressure is pre-calculated with some sophisticated software on the ground, its precise value may be inaccurate since its values is measured from the center of mass of the spacecraft which itself includes uncertainties. But the projected areas of the spacecraft are relatively well-known compared to other aerodynamic parameters mentioned above. Therefore, online parameter estimation method may be employed to estimate these slowly changing parameters in real-time when we know that there is not a venting leak acting on the spacecraft. But the parameter estimation performance depends heavily on the observability of the parameters of interest. Usually in the parameter estimation problem, the state vector is extended by adjoining it with the vector of unknown parameters, as we have done for the vent torque estimation algorithm. In this section, online parameter estimation methods using the least-square approach are derived and the relative observability of the inertia components are investigated.

When the ISS attitude is near the LVLH, the inertia matrix are unobservable even though there are some slight attitude variations due to the time varying aerodynamic torque. Assuming that the aerodynamic parameters are known, the inertia matrix observability in an ideal LVLH fixed mode can be shown from the following equations:

$$\begin{aligned} J_{23} &= \frac{1}{4n^2}(\tau_{aero1} - u_1) \\ J_{13} &= \frac{1}{3n^2}(u_2 - \tau_{aero2}) \end{aligned}$$

$$J_{12} = \frac{1}{n^2}(u_3 - \tau_{aero3}) \quad (80)$$

where the constant angular rate $\boldsymbol{\omega} = [0 \ -n \ 0]^T$ and the constant attitude quaternion $\mathbf{q} = [0 \ 0 \ 0 \ 1]^T$ are substituted in the rotational Euler equations of motion. The quantities $\tau_{aero i}$ and u_i are the i^{th} component of the aerodynamic torque and the control torque input, respectively, and J_{ij} is the ij^{th} inertia matrix element. The spacecraft is assumed to be rotating in an Earth-pointing mode with a constant attitude angular rate $n = 0.0011$ rad/sec. We can see from Eqs. (80) that among the six inertia components, only the products of inertia (J_{23} , J_{13} and J_{12}) show up due to the presence of the gravity-gradient torque. But note that the control input \mathbf{u} and the aerodynamic torque $\boldsymbol{\tau}_{aero}$ have small values with the same order of magnitude. Therefore, exact knowledge of the aerodynamic and control input torque are needed to directly calculate the product of inertias, which is not feasible in a real world.

A numerical test is done with the batch least-square method to check the observability conditions in the LVLH fixed attitude mode. The assumptions are: 1) perfect measurements of the attitude, angular rate, control input and the angular acceleration are available, 2) perfect knowledge of the aerodynamic torque, 3) no other disturbances besides aerodynamic and gravity-gradient torque are present. The solution of the least-square method for the estimation of the inertia matrix is as follows:

$$\hat{\mathbf{x}} = (H^T H)^{-1} H^T \tilde{\mathbf{y}} \quad (81)$$

where $\hat{\mathbf{x}}$ is a 6-dimensional vector containing the elements of the inertia matrix as

$$\hat{\mathbf{x}} = \underline{\mathbf{J}} = [J_{11} \ J_{22} \ J_{33} \ J_{23} \ J_{13} \ J_{12}]^T \quad (82)$$

and the H and the $\tilde{\mathbf{y}}$ are quantities known from the measurements and the control inputs. Note that a linear parametrization of the equations of motion is needed to use the batch least-square method. The Euler equations can be linearly parameterized with respect to the unknown inertia components as

$$\begin{aligned} -\mathbf{u} + \boldsymbol{\tau}_{aero} &= J\dot{\boldsymbol{\omega}} + \boldsymbol{\omega} \times J\boldsymbol{\omega} - 3n^2 \mathbf{C}_3 \times J\mathbf{C}_3 \\ &= [D_1(\dot{\boldsymbol{\omega}}) + D_3(\boldsymbol{\omega}) - 3n^2 D_3(\mathbf{C}_3)] \underline{\mathbf{J}} \\ \tilde{\mathbf{y}} &= H \underline{\mathbf{J}} \end{aligned} \quad (83)$$

where the matrices D_1 and D_3 are defined as in [7].

The quantity $H^T H$ should be strictly positive definite since its inverse appears in Eq. (81) to solve the unknown parameters $\hat{\mathbf{x}}$. In practice, we require $H^T H$ to be well-conditioned, a useful measure of the condition of a matrix is the condition number. The condition number varies from 1 for an orthogonal matrix to infinity for a singular matrix. From a numerical simulation, when all six components of inertia matrix are solved using the Eq. (81), the condition number of the $H^T H$ is 1.7×10^{10} resulting in the divergence of the solution. The relative observability among the inertia components is analyzed using the eigenvalue and eigenvector decomposition of

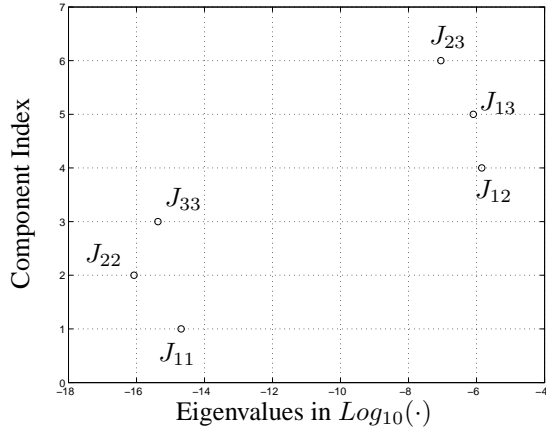


Figure 9. Relative Observability of Inertia

the $H^T H$ matrix, which is shown in Fig. 9. In this figure we can see the relative observability of the inertia components. For example, J_{11} is the maximum component of the eigenvalue which corresponds to the eigenvalue around 10^{-15} . As expected the three products of inertia, which have their eigenvalues near 10^{-6} are the most observable components among the elements, whereas the three moments of inertia have their magnitude near 10^{-15} which is 10^{-9} smaller than those of the products of inertia. A simulation has been done to estimate the product of inertia with a batch least-square method, and the results are shown in Fig. 10 (where the results are calculated at regular instant of time with the cumulative measurements). The three components converge very

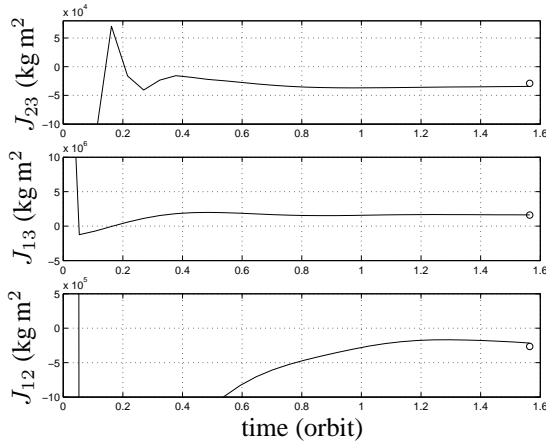


Figure 10. Inertia Product Estimates Using Least-Square Method

fast within an orbit to its true values as expected. The corresponding condition number is 16 which is much smaller than the previous simulation case revealing that the $H^T H$ is now a well-conditioned matrix. But note that the presence of noise in the measurements makes the products of inertia unobservable. For the real-time estimation of the inertia, the UF approach is preferred over the EKF since the expected error is lower and it avoids the derivation of complicated Jacobian matrices with its robustness in the presence of large initial

state uncertainty. Also, the inertia estimation should be performed only when an attitude maneuver is present to enhance the observability of the parameters.

6. LEAK LOCALIZATION

Once a vent torque \mathbf{d}_{vent} is estimated by the real-time filter, the next step involves determining the position vector \mathbf{r}_{vent} , which is the moment arm of the vent torque satisfying

$$\mathbf{d}_{vent} = \mathbf{r}_{vent} \times \mathbf{F}_{vent} \quad (84)$$

In the above equation, the vent torque \mathbf{d}_{vent} and the magnitude of \mathbf{F}_{vent} are known by the estimation algorithms. The overall steps for locating a leak on the ISS are as follows:

1. Model the 3 dimensional geometric surfaces of the pressurized parts of the spacecraft.
2. Estimate the vent torque and magnitude of the vent thrust.
3. Slice the 3-D surfaces of the pressurized modules with a plane perpendicular to the direction of the vent torque so that this plane comprises the center of mass of the spacecraft. From the fundamental definition of torque, a torque about the center of mass of a rigid body is perpendicular to the plane comprising the vectors \mathbf{r}_{vent} and \mathbf{F}_{vent} . So, \mathbf{r}_{vent} , \mathbf{F}_{vent} and the center of mass are all in the same plane normal to the direction of the vent torque. Denote this plane by τ . The intersection between the plane τ and the surface of the spacecraft produces contours.
4. With the assumption that the vent thrust is normal to the tangent plane of the partial section on the ISS surface where the leak occurs, calculate the gradient vectors (direction normal vectors) of the points that make up the sliced contours obtained in Step 3.
5. Multiply the magnitude of the vent thrust estimated in Step 1 with all gradient vectors calculated in Step 4.
6. Since the position and gradient vectors of all the points making the sliced contours are known, calculate the resulting torque at each point on the contours.
7. From the torques obtained for each point in Step 6, select the torques that are closest to the estimated torque (within an error bound) and check their points on the contours.

The actual geometric structure of the station eliminates many of the possible solutions; however, multiple solutions may still exist. In this case further assumptions can be made, such as the probability of impacts by the debris or small meteorites is low on the aft and nadir facing surfaces since these surfaces are shaded by other structures. Also, the leak localization method based on the attitude response may be combined with the conventional leak localization methods. For example, if the solution shows two leaks situated at two different modules then only one hatch closure between any of these modules is needed to check which one of the two modules leaks. Furthermore, visual inspections by the crew may narrow the possible leak solutions.

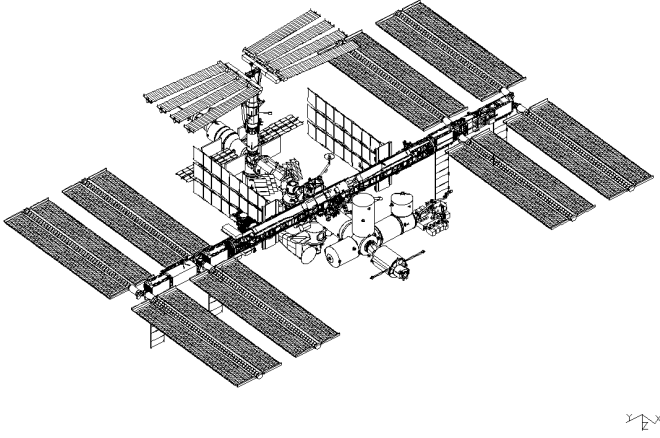


Figure 11. ISS Assembly Stage 16A

7. NUMERICAL SIMULATION

A numerical algorithm coded in MATLAB has been developed to test the performance of the leak localization method for various situations. For the simulation, the ISS assembly Stage 16A is considered (see Fig. 11). In this research, MATLAB 3-D surface models of the pressurized segment of the ISS Stage from 4R to UF-7 have been developed based on the data provided in Ref. [1]. The isentropic depressurization process of the air inside the ISS is assumed. The mass and aerodynamic properties of the ISS are provided in Ref. [1]. The inertia J is given by

$$J = \begin{bmatrix} 127908568 & 3141229 & 7709108 \\ 3141229 & 107362480 & 1345279 \\ 7709108 & 1345279 & 200432320 \end{bmatrix} (\text{kg m}^2) \quad (85)$$

The centers of pressure are $\rho_{cp_x} = [0, -0.355, -0.927]^T$ m, $\rho_{cp_y} = [-7.94, 0, -1.1]^T$ m and $\rho_{cp_z} = [1.12, 0.247, 0]^T$ m in the Space Station Analysis Coordinate System (SSACS) with respect to the center of mass. The components x , y and z represent the three orthogonal axes of the ISS body fixed frame [1]. The reference projected areas are $S_x = 967 \text{ m}^2$, $S_y = 799 \text{ m}^2$ and $S_z = 3525 \text{ m}^2$.

The Global Positioning System (GPS) attitude-sensor measurement-error standard deviation is given by $\sigma_q = 0.5$ deg, and the ring-laser gyro sensor measurement-error standard deviation is given by $\sigma_\omega = 4 \times 10^{-6}$ deg/sec [19]. The measurement-error standard deviation of the internal pressure is given by $\sigma = 0.1$ mmHg. For the depressurization of the air inside, the initial internal temperature and pressure are set to $T_0 = 21^\circ \text{ C}$ and $P_0 = 1$ atm, respectively. The back pressure is assumed to be $P_B = 0$ atm, and the volume of the entire pressurized system for ISS 16A is $V = 867.2 \text{ m}^3$. Finally, an inertia uncertainty of 3% is added to the true J .

Simulations are done for 100 seconds from the start of the leak. Figure 12 shows the estimate of the leak hole area using the Kalman filter algorithm. The true leak hole area A

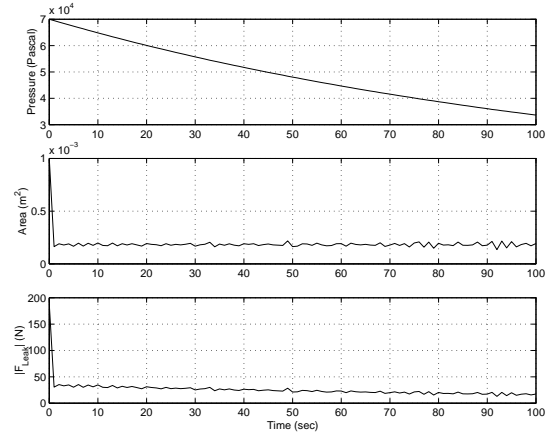


Figure 12. Vent Thrust Magnitude and Hole Area Estimate

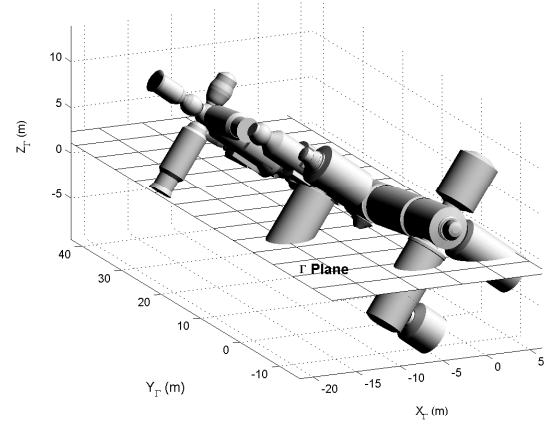


Figure 13. Slicing 3-D Surface Model with Plane τ

is $1.8241 \times 10^{-4} \text{ m}^2$. As seen from this figure the Kalman filter accurately estimates the leak hole area. The vent thrust magnitude is then computed with the internal pressure measurement and the estimate of the hole area.

For the first simulation a leak is assumed on a module shown in Fig. 13. The sliced plane τ with contours in 3-D is shown in Fig. 14. Using the leak localization approach a single leak has been determined for this simulated case, depicted in Fig. 15. The estimated position is marked with a \circ , the true position of a leak is marked with a $*$ for comparison, and the center of mass is marked with a $*$ on the plane τ . Slicing of the 3-D surface is performed at the end of the simulation ($t = 100$ sec). If no errors are present in the assumed model and if the assumptions made so far are perfectly satisfied, then the closest torque yielding the point to the estimated vent torque is the true leak point. But because of sensor inaccuracies and modelling errors in the inertia, the estimated vent torque may deviate from the true value. Therefore, an upper error-bound should be set when selecting points that yield the torque closest to the estimated vent torque. For the case shown in Fig. 15, we conclude that the leak occurs on the contour line labelled 8, which corresponds to the Kibo JEM pressurized module.

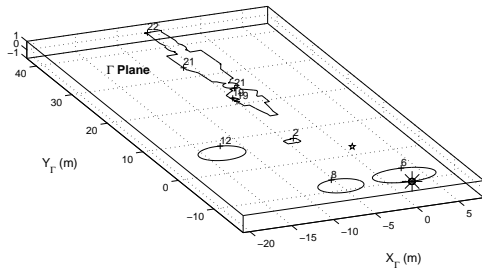


Figure 14. Sliced Plane τ with Contours in 3-D

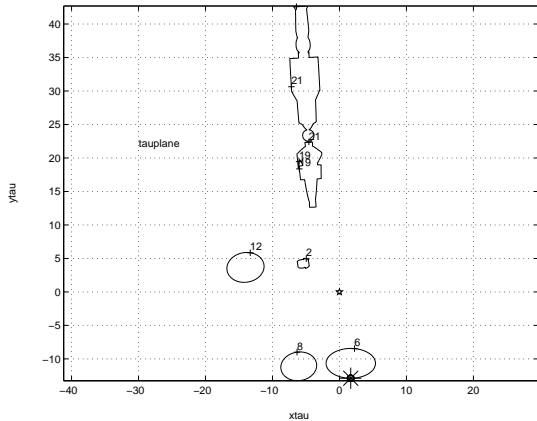


Figure 15. Contours on Plane τ with Possible Leak

In this simulated case, the leak location is well estimated using the new localization method.

Another simulation has been done where multiple locations may result from the given estimated vent torque. In this case the estimated leak locations are spread over several modules, as shown in Fig. 16. The locations P_1 , P_2 and P_3 are possible leak candidates (the true leak point is situated near P_1). But since P_1 and P_2 are on the same module, a crew person only needs to close one hatch between the module labelled 20 and the module labelled 19 to verify which one of the two modules has a leak. This is accomplished by measuring the internal pressure drop rate or using visual inspections of the estimated leak points. If the leak hole is due to space debris or small meteorite punctures, then the aft and nadir facing surfaces of the ISS have little possibility to be impacted. This is also true for locations where regions are protected by other structures, as is the case for point P_3 . Therefore this point is not a likely candidate for the leak.

Initial results indicate that the leak localization method may be sensitive to modelling errors, such as the spacecraft mass properties and aerodynamic parameters. Also the effect of the disturbance torque caused by the pressure of the impingement of the leaking air plume on nearby surfaces may be a critical

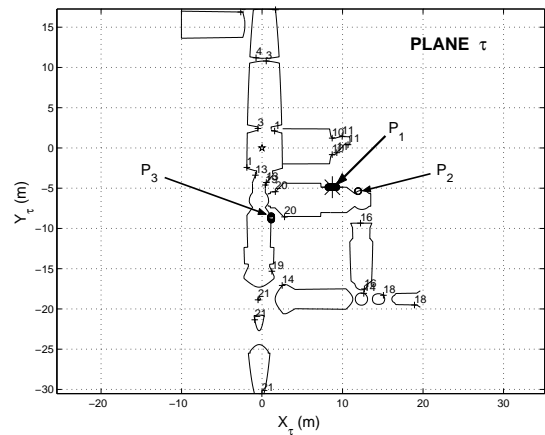


Figure 16. Contours on Plane τ with 3 Possible Leaks

source of disturbance when a leak occurs. Because of inherent complexities, analyzing these effects may be difficult.

8. EXPERIMENTAL VALIDATION

In this chapter, we will show the effects of the air vent with the actual measurements taken from the ISS. A direct test of the current leak localization method is not possible, but it is still useful to test the actual influence of the vent torque on the ISS attitude for an airlock depressurization, which occurred during the Extravehicular Activity (EVA) when the shuttle was docked with the ISS in February 2001. The first part of this chapter will show the results of the disturbance torque estimation with the actual attitude data of the ISS in the TEA mode taken in January 2002. Next, we will show the Space Shuttle airlock depressurization effects on the attitude with the actual data taken in February 2001.

Disturbance Estimation Test

In this section, the disturbance estimation algorithm tests using the UF and the EKF are done for the actual attitude and rate data downloaded in January 2002 for the ISS assembly stage UF1. The quality of the raw data is not ideal to check the disturbance estimation algorithm because of the presence of large measurement gaps within several portions of orbits. These data gaps problem can be avoided if the disturbance estimation algorithm operates online onboard the ISS. All the data gaps in the actual data are interpolated at 1 Hz for the estimation purpose. Figures 17 and 18 show the attitude and the CMG control input measurements profile of the ISS, respectively. From Fig. 17, we can see that the TEA is about -1° for roll, -8° for pitch and -10° for yaw axis, also note that the attitude sensor noise is much smaller than the GPS attitude noise standard deviation of 0.5° since the attitude were measured by the Russian star tracker (the GPS attitude data were not available for the ISS assembly stage UF1). From Fig. 18, the CMG momentum buildup does not occur in all three axes, meaning that the spacecraft attitude is in the TEA mode. Figures 19 show the noisy angular rate measurement. In the attitude dynamics model, the aerodynamic torque is in-

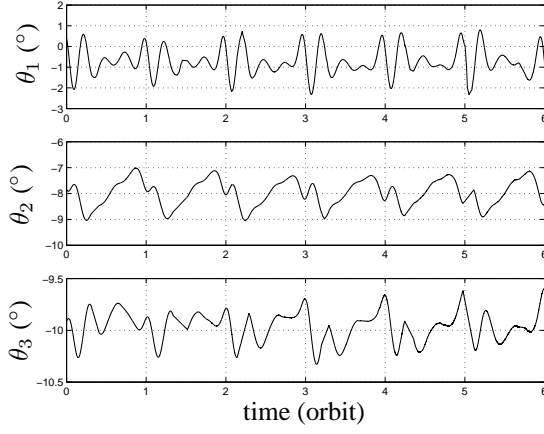


Figure 17. Attitude in Roll, Pitch and Yaw

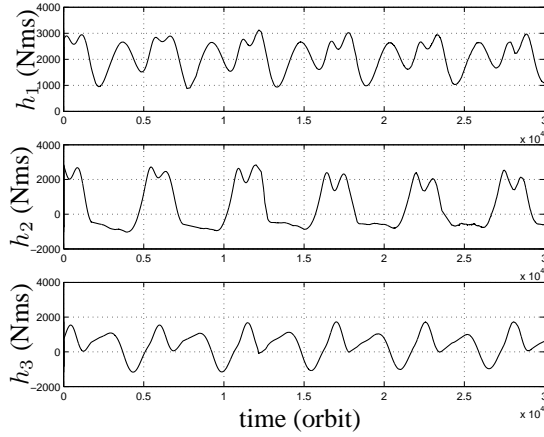


Figure 18. CMG Angular Momentum

tentionally omitted, so that the aerodynamic torque prevails the residual torque. To test the performance of the current disturbance torque estimation approach, the residual torque is calculated using a finite-difference method as

$$d_f(t) = \frac{\mathbf{H}(t + \Delta t) - \mathbf{H}(t)}{\Delta t} + J^{-1}[\mathbf{H}(t) - \mathbf{h}(t)] \times \mathbf{H}(t) - 3n^2 \mathbf{C}_3(\mathbf{q}(t)) \times J \mathbf{C}_3(\mathbf{q}(t)) \quad (86)$$

where Δt is the sampling time which is 1 sec. In Eq. (86) all the quantities come directly from the measurement without any filtering process. The resulting $d_f(t)$ is shown in Fig. 20 where we can clearly see the interpolated part of the measurement data. But by looking at this figure not much information can be obtained since the plots are too noisy to analyze. Figure 21 is the residual torque estimated using the UF approach where much of high frequency noises is filtered out compared to Fig. 20. But since the true residual torque is unknown, the Fast-Fourier Transform (FFT) method is employed to extract the magnitudes and their corresponding frequencies from $d_f(t)$. Figure 22 shows the comparison between the FFT of the $d_f(t)$ and the FFT of the estimated value, $\hat{d}(t)$, using the UF. In this figure, it is hard to discern

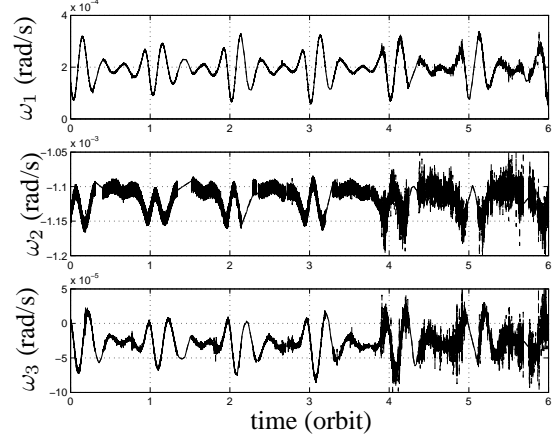


Figure 19. Angular Rate Measurement

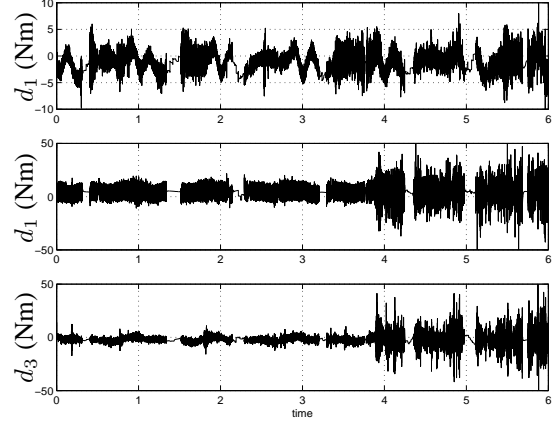


Figure 20. Disturbance Torque from Finite Difference Method

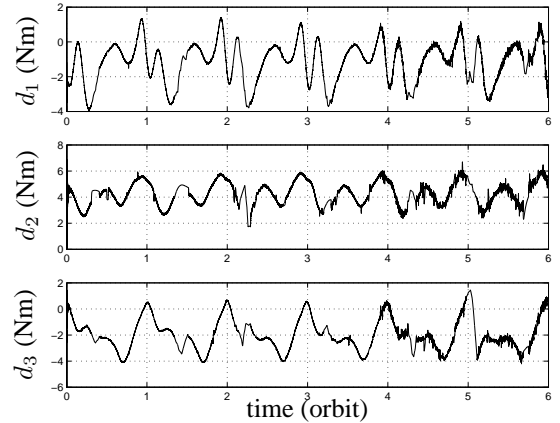


Figure 21. Disturbance Torque Estimate

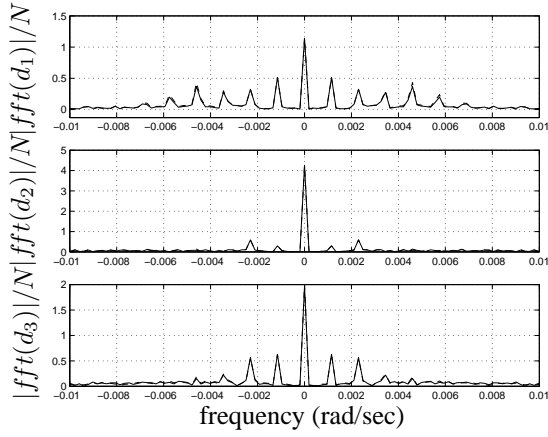


Figure 22. Comparison of Estimate and Finite Difference Value of Disturbance Torque FFT

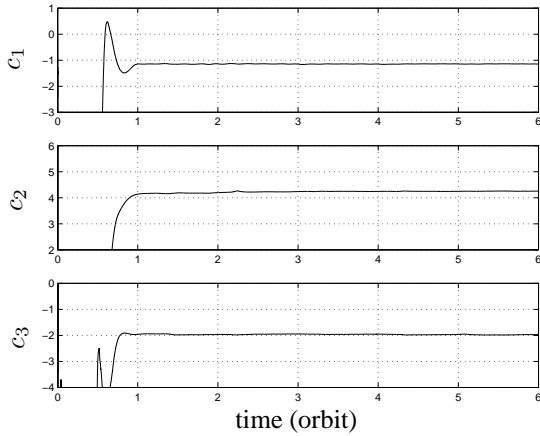


Figure 23. Estimates of c Using KF

the two lines since they overlap perfectly each other, meaning that the low frequency components are all extracted from the noisy measurements without any significant attenuation in their signal powers. Every component of the residual disturbances constitute of a bias plus some signals whose frequencies are multiples of the orbital frequency (0.00113 rad/s). The bias plus signals up to 2 times of the orbital frequency are dominant for d_2 and d_3 . But for d_1 , periodic signals with frequency up to 5 times the orbital frequency have equivalent magnitude compared to each other. Since the inertia uncertainty error has little effect on the attitude dynamics in the TEA mode, the residual torque can be thought as the aerodynamic torque plus some small magnitude of unmodeled disturbances. The frequency at one-time of the orbital frequency is caused by the diurnal bulge of the atmosphere density, whereas the two-times of orbital frequency component is produced by the seasonal effects, which is latitude dependent, and the solar arrays rotational effects. But in the ISS UF1 only one of two U.S. solar arrays was fully functional because one of the solar array α gimbal had a mechanical problem. The cyclic residual torque shown in Fig. 21 can be fitted to the polynomials at integer multiples of the orbital frequency, n , by using the batch least-square or real-time Kalman filter.

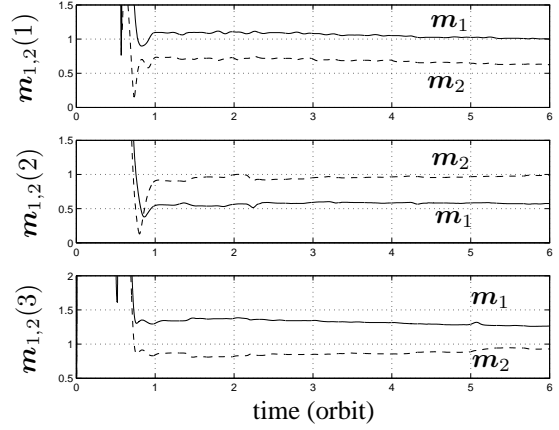


Figure 24. Estimates of m_1 and m_2 Using KF

The polynomial equations can be expressed as follows:

$$\begin{aligned}
 \mathbf{d}(t) &= \mathbf{c} + \mathbf{a}_1 \cos(nt) + \mathbf{b}_1 \sin(nt) + \mathbf{a}_2 \cos(2nt) \\
 &+ \mathbf{b}_2 \sin(2nt) + \mathbf{a}_3 \cos(3nt) + \mathbf{b}_3 \sin(3nt) \\
 &+ \mathbf{a}_4 \cos(4nt) + \mathbf{b}_4 \sin(4nt) \\
 &= \mathbf{c} + \mathbf{m}_1 \cos(nt + \phi_1) + \mathbf{m}_2 \cos(2nt + \phi_2) \\
 &+ \mathbf{m}_3 \cos(3nt + \phi_3) + \mathbf{m}_4 \cos(4nt + \phi_4) \quad (87)
 \end{aligned}$$

where $\mathbf{m}_1 \sim \mathbf{m}_4$ for each element $i = 1, 2, 3$ are defined as

$$\mathbf{m}_1(i) = \sqrt{\mathbf{a}_1(i)^2 + \mathbf{b}_1(i)^2} \quad (88)$$

$$\mathbf{m}_2(i) = \sqrt{\mathbf{a}_2(i)^2 + \mathbf{b}_2(i)^2} \quad (89)$$

$$\mathbf{m}_3(i) = \sqrt{\mathbf{a}_3(i)^2 + \mathbf{b}_3(i)^2} \quad (90)$$

$$\mathbf{m}_4(i) = \sqrt{\mathbf{a}_4(i)^2 + \mathbf{b}_4(i)^2} \quad (91)$$

The estimation results of $\mathbf{m}_1 \sim \mathbf{m}_4$ using the KF are shown in Figs. 23, 24 and 25. We can see that the estimate results of c and $\mathbf{m}_1 \sim \mathbf{m}_4$ are consistent with the results shown in Fig. 22. Note that $\mathbf{m}_1 \sim \mathbf{m}_4$ should be multiplied by two when comparing with the results of the FFT. The quantities of second components of \mathbf{m}_3 and \mathbf{m}_4 are not as prominent as can be seen from the second plot of Fig. 22. These c and $\mathbf{m}_1 \sim \mathbf{m}_4$ can be subtracted from the overall residual torque when a vent torque is present. But an assumption should be made that the spacecraft does not deviate much from the attitude where $\mathbf{m}_1 \sim \mathbf{m}_4$ are estimated.

A proposed method involves determining a residual model error, which includes all the aforementioned effects, using the UF filter when it is known that a leak does not occur. Then, assuming that the residual error is small for the next orbit, this model error is subtracted from the new estimated model error in the next orbital pass. If no leak is determined, then a new residual error is determined and the process continues until a leak is found.

Airlock Depressurization

The effects of the air vent on the attitude of the ISS assembly Stage 5A with the mated Space Shuttle (STS-98) is investigated in this subsection (see Fig. 26 adapted from [1]).

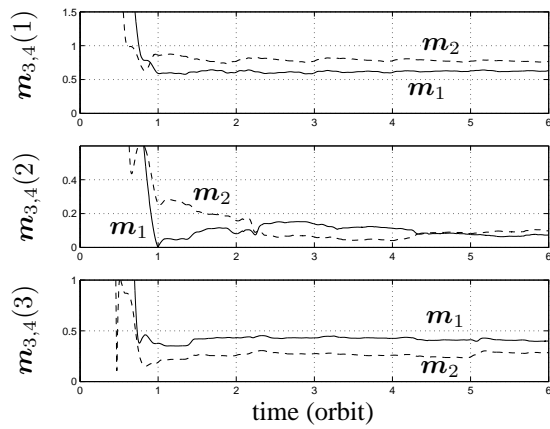


Figure 25. Estimates of m_3 and m_4 Using KF

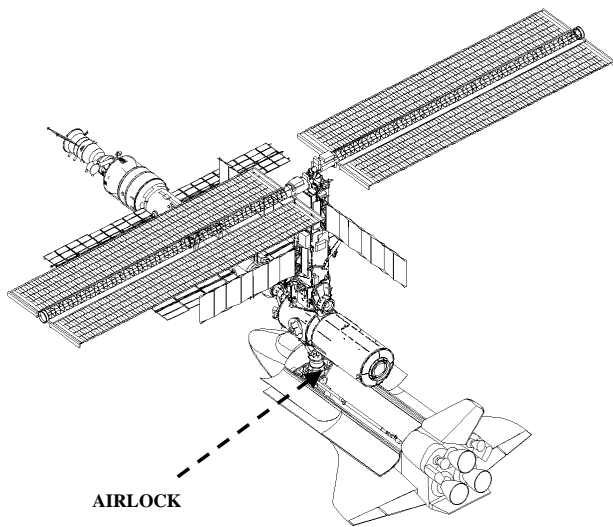


Figure 26. ISS mated with Space Shuttle Atlantis, Stage 5A Intermediate 2

The purpose of this section is to estimate the torque and the magnitude of the thrust caused by the air vent from the depressurization of the Space Shuttle airlock for the preparation of extravehicular activity (EVA) of the crew. The actual data are recorded from 2001, 045, 09 h 30 min (GMT) through 2001, 045, 15 h 40 min (GMT), and airlock depressurization started around 14 h 30 min. Because a T-shaped valve is used (see Fig. 27), where air is vented on opposite sides of the valve structure in the direction of $\pm z$ (third) body axis, the net thrust should be nullified in theory. But if the expelled air is not uniform at both openings a net thrust may occur. In the present case, from Fig. 28, the CMG momentum buildup occurs during the pressurization process which means that the net thrust is not cancelled.

In preparation for an EVA, two stages are needed to depressurize the Space Shuttle external airlock:

1. The airlock is depressurized from 703 hPa to 345 hPa. The valve is open until 345 hPa is reached and then closed

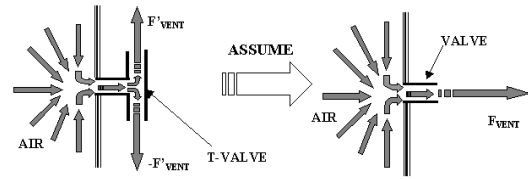


Figure 27. External Airlock of Space Shuttle and Depress Valve

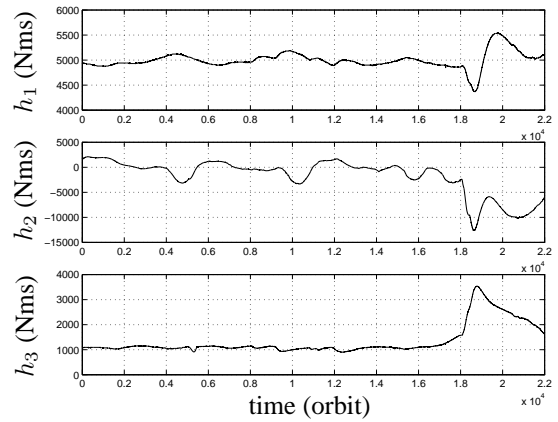


Figure 28. CMG Angular Momentum

to maintain 345 hPa.

2. The valve is reopened with the valve diameter increased to depressurize the airlock from 345 hPa to 0 hPa.

The first plot of Fig. 29 shows the temperature measurement and the pressure profile in the airlock. The airlock depressurization occurs at $t = 18400$ sec (note that $t = 0$ corresponds to $t = 2001, 045, 00$ h 00 min 00 sec in GMT). The magnitude of the thrust caused by the venting air is estimated based on the following assumptions:

1. Depressurization of the airlock follows an isothermal pro-

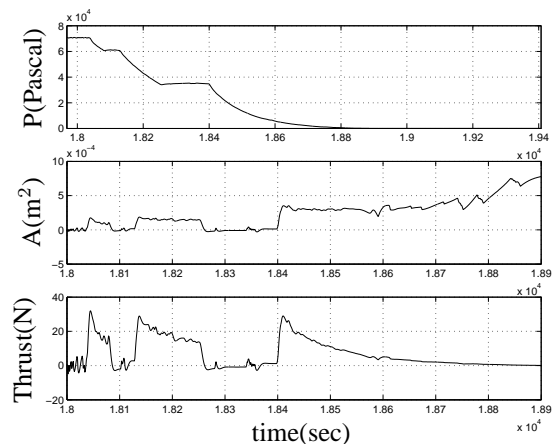


Figure 29. Pressure, Hole Area and Vent Thrust Estimate

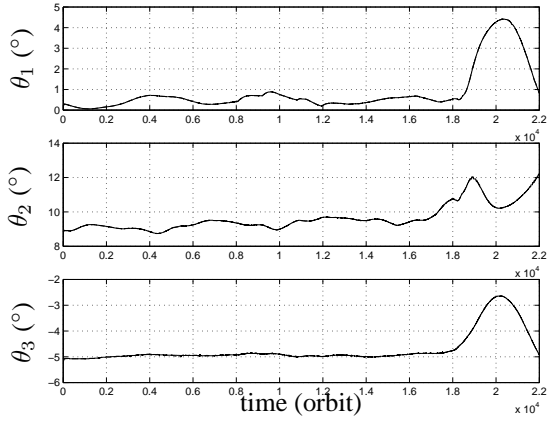


Figure 30. Attitude in Roll, Pitch and Yaw

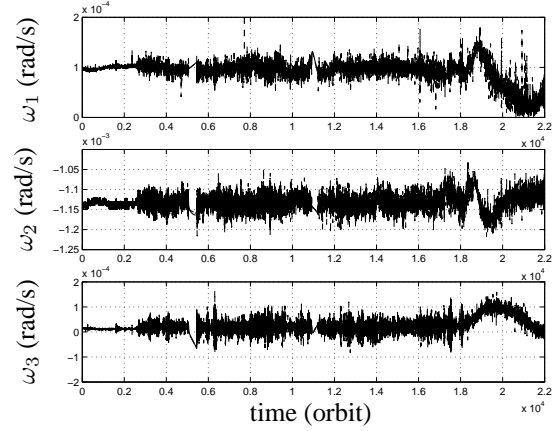


Figure 31. Angular Rate Measurement

cess based on the internal temperature history.

2. A single straight opening valve is used (although a T-shaped valve is used in reality).
3. No air flow decelerations occur inside the valve ($dA = 0$), but the hole area A is not required to be a constant.

Only the upper bound magnitude of the vent thrust can be given because of the assumption made in 2. We can assume that the temperature inside the airlock is nearly constant around 18°C based on the temperature measurement taken inside the airlock. Therefore, we can infer that the isothermal air model is a better representation of the physics of the air depressurization inside the airlock. Figure 29 shows the results obtained from the EKF algorithm. The figures are rescaled to show the depressurization part in detail. The pressure data closely follows the predicted depress process of the EVA explained earlier. The estimated hole area varies between $1 \times 10^{-4}\text{ m}^2$ to $3 \times 10^{-4}\text{ m}^2$, which corresponds to 0.56 cm (0.22 in) and 1 cm (0.4 in) in hole radius, respectively. Note that the computed valve area does not reveal the actual one because of the assumptions made in 2. Therefore from the results shown in Fig. 29, only an upper bound of the exit area of the valve can be obtained. Figures 30 shows the attitude measurements profile of the ISS. The angular rate measurement and its estimated value using the UF approach are shown in Figs. 31 and 32, respectively.

The vent torque estimation results using the UF approach is shown in Fig. 33. In this figure, we can see that negative torques occur in d_1 and d_2 , and a positive torque arises in d_3 . It may be the results of the plume impingement effects of the venting air on the nearby surfaces of the spacecraft structures. For the analyses of the plume impingement effects, a computational fluid dynamics (CFD) method should be performed which is outside of the scope of this paper. But we can infer from Fig. 27 that the presence of the radiator (in the direction of the y body axis) on the left-hand side of the figure might have impinged with the venting plume reflected by the Shuttle bay.

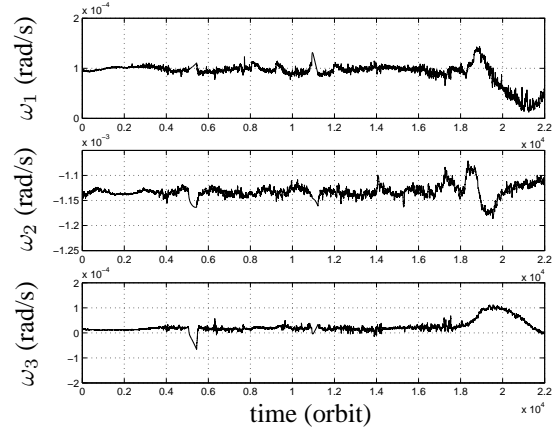


Figure 32. Angular Rate Estimate

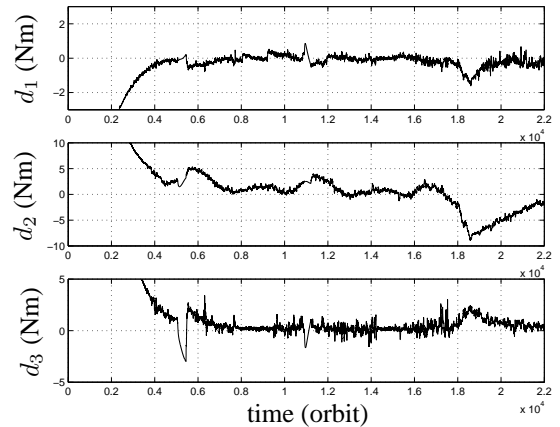


Figure 33. Disturbance Torque Estimate

This is not ideal case to test the leak localization method since the external airlock of the Space Shuttle is situated inside the Space Shuttle cargo bay with the depressurization valve at its bottom part (valve location: $[10.34 \ 0.865 \ 10.568]^T$ m), which probably interacted with surfaces near the airlock valve. The computation of the stream of the vent plume inside the shuttle cargo bay can only be performed with the traditional computational fluid dynamics (CFD) which is out of scope of this paper. Furthermore the geometry of the T-shaped valve makes the analysis more complicated. However, the obtained results are consistent with intuitive assumptions.

9. CONCLUSIONS

In this paper a new leak localization method using the attitude response is developed for the ISS. The reaction thrust arising from a vent due to air leak are calculated using the isentropic nozzle theory. Also, the isentropic and isothermal depressurization models have been considered to describe the depressurization process of the pressurized module. Based on these models, the vent thrust magnitude is estimated by employing the KF. The UF approach is used for the purpose of estimating the attitude and residual disturbance torque. The UF approach is preferred over the EKF since the expected error is lower and it avoids the derivation of complicated Jacobian matrices. The superior performance of the USQUE over the conventional EKF approach in the attitude estimation problem has been shown when the initial attitude estimate error has large uncertainties.

In the ISS, an incorrect inertia may be the primary source of uncertainty in estimating the vent torque. Also, unlike the deterministic gravity-gradient, the precise determination of the aerodynamic torque is very difficult due to the lack of the knowledge of the drag mechanism in rarefied atmosphere activities. But since the upper bound of the aerodynamic torque is known, the vent torque which is much larger than the aerodynamic torque has no much effect on the vent torque estimation results. It has been shown with the batch least-square analysis that the inertia matrix is unobservable when the ISS is near the LVLH. Therefore, to enhance the observability of the unknown parameters, an appropriate attitude maneuver should be performed. For the real-time inertia parameter estimation, the robustness in the presence of large initial state uncertainty and no necessities of the Jacobian derivations may make the UF approach attractive.

The actual geometric structure of the station eliminates many of the possible solutions; however, multiple solutions may still exist. In this case further assumptions should be made, such as the probability of impacts by the debris or small meteorites is low on the aft, nadir facing surfaces and some parts of the surfaces which is not likely to have leak. Also, the leak localization method based on the attitude response may be combined with the conventional leak localization methods. For example, if the solution shows two leaks situated at two different modules then only one hatch closure between any of these modules is needed to check which one of the two mod-

ules leaks. Furthermore, visual inspections by the crew may narrow the possible leak solutions.

Numerical results showed that the proposed leak localization method determines the location of the leak rapidly and precisely. Furthermore, actual test data from a depressurization of the Space Shuttle airlock indicates that the proposed method has the potential to accurately estimate the leak hole size and venting force magnitude.

The advantages of this localization method are: no other devices are needed besides pressure gauges, spacecraft attitude and rate sensors, and relatively fast leak localization can be achieved compared to the conventional leak localization method proposed for the ISS. Also this localization method not only determines the possible leaking modules but also the possible locations of a leak hole within the surfaces of the modules, which may be critical to allow for repairs rather than sealing off the module or performing a station evacuation.

10. ACKNOWLEDGEMENTS

This work has been supported by a grant from United Space Alliance (contract number C00-00109). This support is greatly appreciated.

REFERENCES

- [1] *International Space Station On-Orbit Assembly, Modeling, and Mass Properties Databook: Design Analysis Cycle Assembly Sequence, JSC-26557, Revision J*, Lockheed Martin, Houston, TX, 1999.
- [2] *Protecting the Space Station from Meteoroids and Orbital Debris*, National Research Council, Washington, DC, 1997.
- [3] Julier, S. J., Uhlmann, J. K., and Durrant-Whyte, H. F., "A New Approach for Filtering Nonlinear Systems," *American Control Conference*, pp. 1628-1632, Seattle, WA, 1995.
- [4] Crassidis, J. L. and Markley, F. L., "Unscented Filtering for Spacecraft Attitude Estimation," submitted to *Journal of Guidance, Control, and Dynamics*.
- [5] Wan, E. and van der Merwe, R., "The Unscented Kalman Filter for Nonlinear Estimation," *Proceedings of IEEE Symposium 2000*, pp. 153-158, Lake Louise, Alberta, Canada, Oct. 2000.
- [6] Bishop, R. H., Paynter, S. J., and Sunkel, J. W., "Adaptive Control of Space Station During Nominal Operations with CMGs," *IEEE Conference on Decision and Control*, Brighton, England, Dec. 11-13 1991.
- [7] Carter, M. T., *Real-Time Analysis of Mass Properties*, Dissertation, Texas A&M University, College Station, February 1999.
- [8] Paynter, S. J., *Adaptive Control of the Space Station*, M.s. thesis, University of Texas, Austin, December

1992.

- [9] Crassidis, J. L., Markley, F. L., Anthony, T. C., and Andrews, S. F., "Nonlinear Predictive Control of Spacecraft," *Journal of Guidance, Control, and Dynamics*, Vol. 20, No. 6, Nov.-Dec. 1997, pp. 1096–1103.
- [10] Carter, M. T. and Vadali, S. R., "Parameter Identification for the International Space Station Using Nonlinear Momentum Management Control," *AIAA-97-3524*, August 1997.
- [11] Sonntag, R. E., Borgnakke, C., and Wylen, G. J. V., *Fundamentals of Thermodynamics*, John Wiley & Sons, Inc., New York, 5th ed., 1998.
- [12] Crassidis, J. L. and Junkins, J. L., "*Optimal Estimation of Dynamic Systems*," CRC Press, Boca Raton, FL, to be published.
- [13] Julier, S. and Uhlmann, J., "A New Extension of the Kalman Filter to Nonlinear Systems," *Int. Symp. Aerospace/Defense Sensing, Simul. and Controls*, Orlando, FL, 1997.
- [14] Lefferts, E. J., Markley, F. L., and Shuster, M. D., "Kalman Filtering for Spacecraft Attitude Estimation," *Journal of Guidance, Control, and Dynamics*, Vol. 5, No. 5, Sept.-Oct. 1982, pp. 417–429.
- [15] Schaub, H. and Junkins, J. L., "Stereographic Orientations Parameters for Attitude Dynamics: A Generalization of the Rodrigues Parameters," *Journal of the Astronautical Sciences*, Vol. 44, No. 1, Jan.-March 1996, pp. 1–20.
- [16] Farrenkopf, R. L., "Analytic Steady-State Accuracy Solutions for Two Common Spacecraft Attitude Estimators," *Journal of Guidance, Control, and Dynamics*, Vol. 1, No. 4, Jul.-Aug. 1978, pp. 282–284.
- [17] Markley, F. L., "Attitude Representations for Kalman Filtering," *AAS/AIAA Astrodynamics Specialist Conference*, Quebec City, Quebec, August 2001, AAS 01-309, pp. 133–152.
- [18] Owens, J. K., Niehuss, K. O., and Vaughan, W. W., "Models for Future Estimation of Thermospheric Densities and Application to Spacecraft Systems," *37th Aerospace Sciences Meeting and Exhibit*, Reno, Nevada, Jan. 1999, AIAA 99-16498.
- [19] *United States Control Module Guidance, Navigation, and Control Subsystem Design Concept*, NASA MSFC-3677, Huntsville, AL, March 1997.



Jong-Woo Kim is the visiting instructor in mechanical and aerospace engineering at University at Buffalo, State University of New York. His research interests include robust control and filtering and astronautics. He received the B.S. and the M.S. degrees from Yonsei University, Seoul, Korea and the Ph.D. degree in aerospace engineering from the Texas A&M University, College Station in 1994, 1996 and 2002, respectively. He is a member of AIAA and AAS.



John L. Crassidis is the Associate Professor in mechanical and aerospace engineering at University at Buffalo, State University of New York since 2001. His research interests include navigation, estimation and control theory. Dr. Crassidis obtained the B.S., M.S. and Ph.D. degrees in mechanical and aerospace engineering from the University at Buffalo, State University of New York in 1989, 1991, and 1993, respectively. He is an associate fellow of AIAA and a member of AAS, ASME, SAE and ASEE.



Srinivas R. Vadali is the Professor in aerospace engineering at Texas A&M University, College Station. His research interests include spacecraft dynamics and control, and optimal control. Dr. Vadali obtained an M.S. degree in electrical engineering from Indian Institute of Science in 1978 and a Ph.D. degree from Virginia Polytechnic Institute and State University in 1983. He is an associate fellow of AIAA.



Adam L. Dershowitz is the flight controller for space station Attitude Determination and Control (ADCO) at United Space Alliance in Johnson Space Center, Houston. His research interests include attitude determination and control. Dr. Dershowitz obtained the B.S., M.S. and Ph.D degrees in aeronautical and astronautical engineering from MIT. He is a senior member of AIAA.